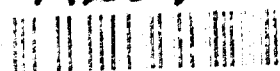
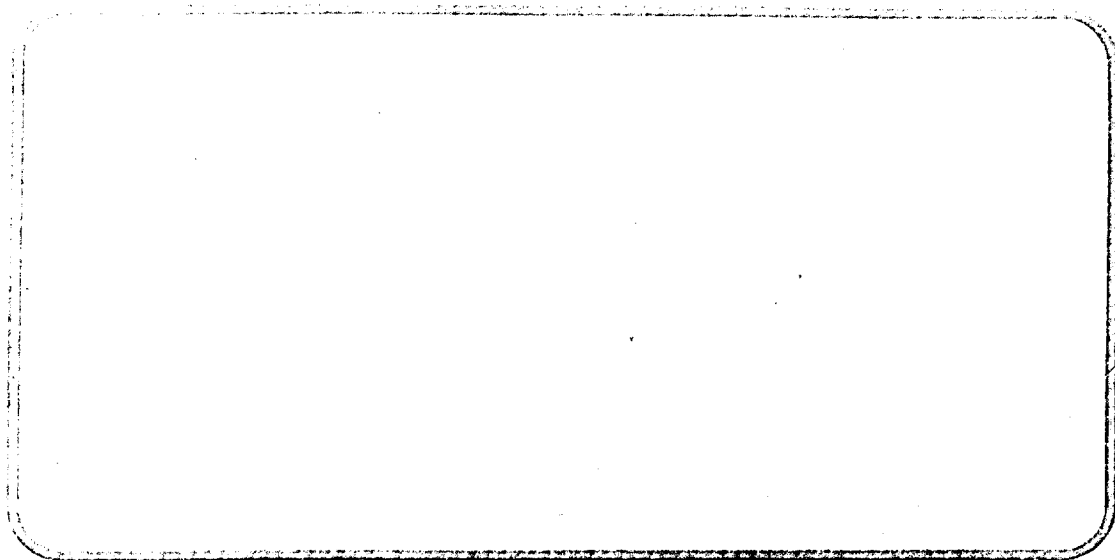


AD-A261 813



93 0137

(2)



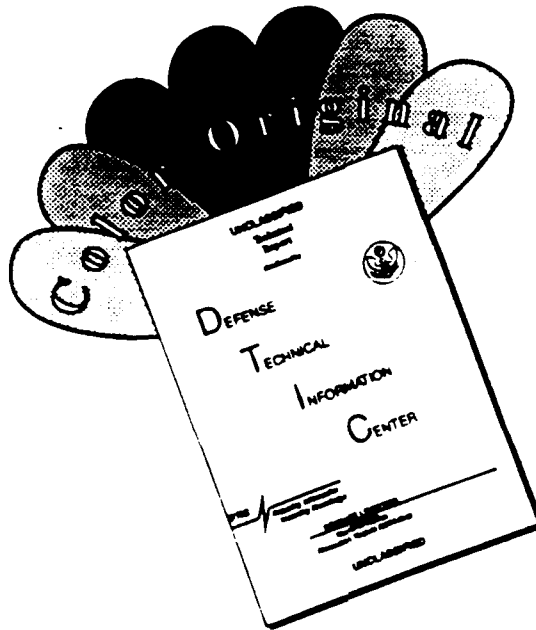
CFD Research Corporation

CFDRC

DTIC
ELECTE
MAR 09 1993
S B D

DISTRIBUTION STATEMENT A
Approved for public release
Distribution Unlimited

DISCLAIMER NOTICE



THIS DOCUMENT IS BEST QUALITY AVAILABLE. THE COPY FURNISHED TO DTIC CONTAINED A SIGNIFICANT NUMBER OF COLOR PAGES WHICH DO NOT REPRODUCE LEGIBLY ON BLACK AND WHITE MICROFICHE.

REPORT DOCUMENTATION PAGE			Form Approved OMB No. 0704-0188	
<small>Public reporting burden for this collection of information is estimated to average 1 hour per response, including the time for reviewing instructions, searching existing data sources, gathering and maintaining the data needed, and completing and reviewing the collection of information. Send comments regarding this burden estimate or any other aspect of this collection of information, including suggestions for reducing this burden, to Washington Headquarters Services, Directorate for Information Operations and Reports, 1215 Jefferson Davis Highway, Suite 1204, Arlington, VA 22202-4302, and to the Office of Management and Budget, Paperwork Reduction Project (0704-0188), Washington, DC 20503.</small>				
1. AGENCY USE ONLY (Leave blank)	2. REPORT DATE Feb. 1993	3. REPORT TYPE AND DATES COVERED Final 7/9/92 - 1/9/93		
4. TITLE AND SUBTITLE Influence of Supercritical Conditions on Pre-Combustion Chemistry and Transport Behavior of Jet Fuels		5. FUNDING NUMBERS PE - 65502F PR - 3005 SA - SS C - F49620-92-C-0030		
6. AUTHOR(S) Anantha Krishnan				
7. PERFORMING ORGANIZATION NAME(S) AND ADDRESS(ES) CFD Research Corporation 3325 Triana Blvd. Huntsville, AL 35805		8. PERFORMING ORGANIZATION REPORT NUMBER CFDRC 4240/2		
9. SPONSORING/MONITORING AGENCY NAME(S) AND ADDRESS(ES) AFOSR/NA 110 Duncan Avenue, Suite B115 Bolling AFB DC 20332-0001		10. SPONSORING/MONITORING AGENCY REPORT NUMBER		
11. SUPPLEMENTARY NOTES				
12a. DISTRIBUTION/AVAILABILITY STATEMENT Approved for public release. distribution unlimited		12b. DISTRIBUTION CODE		
13. ABSTRACT (Maximum 200 words) <p>The objective of the Phase I study was to investigate heat transfer characteristics in supercritical flows. Detailed models were formulated to compute transport properties (such as density, conductivity, viscosity, and specific heat) in the supercritical regime. The models were incorporated into a general purpose Computational Fluid Dynamics (CFD) code capable of modeling flow, heat transfer, and reactions in complex geometries. Two and three-dimensional simulations were performed for supercritical flow and heat transfer in a test cell. Parallel experimental work was done by Professor L.D. Chen at the University of Iowa.</p> <p>The results of the Phase I work show that there is considerable augmentation of heat transfer near the critical point. Also, the large variation in density across the critical point has a significant effect on the near wall profiles of velocity and temperature. Ideal gas approximations of supercritical flows can result in gross errors in predicting heat transfer rates. The development of this supercritical transport model provides a basis for incorporating complex models for pre-combustion chemistry in jet fuels.</p>				
14. SUBJECT TERMS thermal stability, supercritical flows, transport properties, heat transfer		15. NUMBER OF PAGES 51		
		16. PRICE CODE		
17. SECURITY CLASSIFICATION OF REPORT Unclassified	18. SECURITY CLASSIFICATION OF THIS PAGE Unclassified	19. SECURITY CLASSIFICATION OF ABSTRACT Unclassified	20. LIMITATION OF ABSTRACT	

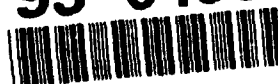
NSN 7540-01-280-5500

Standard Form 298 (Rev. 2-89)
Prescribed by GSA FPMR (41 CFR) 101-11.6

93-04939

53-85

93 3 8 061



CFD Research Corporation

3325 Triana Blvd. • Huntsville, Alabama 35805 • Tel: (205) 536-6576 • FAX: (205) 536-6590



**INFLUENCE OF SUPERCRITICAL CONDITIONS
ON PRE-COMBUSTION CHEMISTRY AND TRANSPORT
BEHAVIOR OF JET FUELS**

Phase I Final Report

by
Anantha Krishnan
CFD Research Corporation
3325 Triana Blvd.
Huntsville, AL 35805

February 1993

CFDRC Report 4240/2

for
Air Force Office of Scientific Research
Bolling AFB, DC 20332

Project Manager: Dr. Julian Tishkoff
Contract Number: F49620-92-C-0030

PREFACE

This report documents the work performed under a six month Phase I SBIR contract (Contract #F498620-92-C-0030) awarded by the Air Force Office of Scientific Research (AFOSR). The AFOSR technical monitor for Phase I was Dr. Julian Tishkoff.

The author would like to express his appreciation to Dr. Julian Tishkoff (AFOSR), Dr. Mel Roquemore (Wright Laboratory) and Dr. Tim Edwards (Wright Laboratory) for participating in technical discussions and providing support and encouragement. Professor L.D. Chen, of the University of Iowa, complemented the Phase I work by performing the experimental component of the study. Dr. Ashok Singhal (President & Technical Director of CFDRC) and Dr. Andrzej Przekwas (Vice President/Research of CFDRC) provided inhouse guidance on this project. The effort of Ms. J. Swann in preparing this report is appreciated.

Accession For	
AS 77-1	<input checked="" type="checkbox"/>
	<input type="checkbox"/>
	<input type="checkbox"/>
Description	
Location/	
Community Codes	
Serial and/or	
Special	
A-1	

TABLE OF CONTENTS

	<u>Page</u>
1. INTRODUCTION	1
1.1 Need for Predicting Supercritical Behavior of Fuels	1
1.2 Phase I Objectives	2
1.3 Phase I Accomplishments	2
1.4 Outline of the Report	4
2. FORMULATION OF SUPERCRITICAL TRANSPORT MODEL	5
2.1 Governing Equations	5
2.2 Calculation of Viscosity	6
2.3 Calculation of Thermal Conductivity	9
2.4 Calculation of Density	10
2.5 Calculation of Enthalpy	11
2.6 Calculation of Specific Heat	12
3. COMPUTATION OF SUPERCRITICAL TRANSPORT FOR SF ₆	14
3.1 Property Variation with Temperature	14
3.2 Supercritical Heat Transfer in a 2-D Channel	17
3.3 Comparison with Ideal Gas Model Predictions	19
3.4 Correlation Between Dimensionless Quantities	20
4. ASSESSMENT OF NATURAL CONVECTION EFFECTS	24
4.1 Case 1 : Gravity Vector $g_y = -9.81 \text{ m/sec}^2$	24
4.2 Case 2 : Gravity Vector $g_y = 9.81 \text{ m/sec}^2$	26
4.3 Case 3 : Gravity Vector $g_x = 9.81 \text{ m/sec}^2$	27
4.4 Case 4 : Gravity Vector $g_x = -9.81 \text{ m/sec}^2$	29
5. EXPERIMENTAL RESULTS FOR SUPERCRITICAL HEAT TRANSFER	32
5.1 Experimental Apparatus	32
5.2 Results and Discussion	34

TABLE OF CONTENTS (Continued)

	<u>Page</u>
6. 3-D COMPUTATIONS OF SUPERCRITICAL TRANSPORT IN THE TEST CELL	38
6.1 Computational Grid and Boundary Conditions	38
6.2 Results of Numerical Simulations	39
6.3 Discussion	39
	45
7. CONCLUSIONS AND RECOMMENDATIONS	46
7.1 Summary of Work Performed	46
7.2 Main Findings from the Phase I Study	47
7.3 Recommendations for Phase II	48
7.4 Phase III Objectives	49
8. REFERENCES	51

LIST OF ILLUSTRATIONS

	<u>Page</u>
Figure 3-1. Variation of Density with Temperature	15
Figure 3-2. Variation of Dynamic Viscosity with Temperature	15
Figure 3-3. Variation of Thermal Conductivity with Temperature	16
Figure 3-4. Variation of Specific Heat with Temperature	16
Figure 3-5a. Schematic of the Channel	17
Figure 3-5b. Computational Grid (100 x 50) for the Channel	17
Figure 3-6. Temperature Distribution ($^{\circ}\text{K}$) in the Channel	18
Figure 3-7. Density (kg/m^3) Distribution in the Channel	18
Figure 3-8. Heat Flux Along the Wall of the Channel	19
Figure 3-9. Density (kg/m^3) Distribution (with Ideal Gas Model) in the Channel	20
Figure 3-10. Schematic of the Channel and Boundary Conditions	20
Figure 3-11. Variation of Heat Flux with Mean Velocity Through the Channel	21
Figure 3-12. Velocity Profile in the Channel	23
Figure 4-1. Pressure Distribution (Pascals) in the Channel for Case 1	24

LIST OF ILLUSTRATIONS (Continued)

	<u>Page</u>
Figure 4-2. Streamline Contours for Case 1	25
Figure 4-3. Heat Flux Along the Channel Wall	25
Figure 4-4. Pressure Distribution (Pascals) for Case 2	26
Figure 4-5. Streamline Contours for Case 2	26
Figure 4-6. Heat Flux Along the Channel Wall.	27
Figure 4-7. Pressure Distribution (Pascals) for Case 3	27
Figure 4-8. Streamline Contours for Case 3	28
Figure 4-9. Heat Flux Along the Channel Wall.	28
Figure 4-10. Pressure Distribution (Pascals) for Case 4	29
Figure 4-11. Streamline Contours for Case 4	29
Figure 4-12. Heat Flux Along the Channel Wall	30
Figure 4-13. Temperature Distribution ($^{\circ}\text{K}$) in the Channel for Case 4	31
Figure 5-1. Schematic of the Experimental Set-Up	33
Figure 5-2. Digitized Image of the Apparatus	33
Figure 5-3. Shadowgraph Images of the Flow in the Test Cell	35
Figure 6-1. Schematic of the Test Cell	38

LIST OF ILLUSTRATIONS (Continued)

	<u>Page</u>
Figure 6-2. Computational Grid (62x44x45) for the Test Cell	40
Figure 6-3. Density Distribution in the Test Cell	41
Figure 6-4. Velocity Field Inside the Test Cell	42
Figure 6-5. Temperature Distribution in the Test Cell	43
Figure 6-6. Heat Flux Distribution on the Heated Surface	44

1. INTRODUCTION

This report documents the work performed during a Phase I SBIR study sponsored by AFOSR. The next phase of work (Phase II) is expected to be two years in duration. The objective of the overall project (Phases I and II) is to develop an experimental/computational approach to model precombustion chemistry and transport behavior of hydrocarbon fuels under supercritical conditions.

The Phase I study focused on addressing heat transfer characteristics under critical and supercritical conditions. The model development and computations were performed at CFDRC by the principal investigator and parallel experimental work was conducted by Professor L. D. Chen at the University of Iowa (under a subcontract from CFDRC).

1.1 Need for Predicting Supercritical Behavior of Fuels

High performance, high speed aircraft of the future will require onboard fuel to act as a heat sink to meet the thermal loads arising from sources such as the engine, the avionics, the air frame, the climate control system, *etc.* Since the pressures in aircraft fuel lines generally exceed the critical pressure of the fuel, the above mentioned thermal loads will cause the fuel temperature to increase beyond the critical temperature, *i.e.*, the fuel will be in the supercritical regime.

The transport and chemical behavior of fuels under supercritical conditions is not well understood. Properties such as density, viscosity, conductivity, diffusivity, specific heat, *etc.* undergo steep variations near the critical point. These variations are expected to alter the heat transfer characteristics of the fuel. The thermal stability of supercritical fuels is of great concern. If the temperature of the fuel exceeds a certain value, the fuel undergoes chemical decomposition to form insolubles such as gums and particle clusters that get deposited on fuel lines, valves, *etc.* Therefore, the heat management has to be done in a temperature range over which the fuel is thermally stable. For JP-8, this range is below 325°F. Advanced fuels such as JP-900 are expected to be thermally stable below 900°F.

Effective heat management in high performance aircraft requires a better understanding of the supercritical transport and chemical properties of the fuel. The Phase I study addressed the issue of supercritical heat transfer. An experimental/computational approach was adopted during Phase I. The Phase II study will involve the analysis of precombustion chemistry and deposit formation under supercritical conditions.

1.2 Phase I Objectives

The specific objectives of the Phase I study were:

- a. to formulate models to calculate supercritical transport properties such as density, viscosity, conductivity and specific heat;
- b. to conduct experiments with Sulfur Hexafluoride (SF_6) as a surrogate fuel and to measure density distributions inside the test cell;
- c. to obtain functional relationships between non-dimensional parameters such as the Nusselt number and the Reynolds number;
- d. to perform preliminary validation of the supercritical transport models; and
- e. to develop recommendations for the Phase II study.

1.3 Phase I Accomplishments

All of the above mentioned objectives were accomplished. The Phase I work resulted in the formulation of a comprehensive supercritical transport model. This model was incorporated into an existing Computational Fluid Dynamics (CFD) code. This has resulted in a unique capability to compute supercritical flow behavior based on local conditions. The modified code was used to simulate heat transfer characteristics over a range of conditions. The results were compared with data obtained from parallel experiments at the University of Iowa. SF_6 was used as a surrogate fuel for the Phase I study.

The specific achievements of the Phase I study are listed below.

- a. A model was formulated to calculate the supercritical transport properties based on the local pressure, temperature and composition. The low pressure properties were calculated from the kinetic theory of gases and appropriate dense gas corrections were used to estimate the properties at supercritical conditions.
- b. The flow inside the test cell was experimentally visualized and shadowgraphs were obtained to show density variations.
- c. Preliminary validation of the model predictions was done by comparing the results against existing data for SF_6 .¹
- d. The supercritical transport model was incorporated into an existing CFD code, REFLEQS (REactive FLOW EQUation Solver). The code was used to compute heat transfer characteristics in a 2-D channel. The results of the supercritical model were compared with ideal gas predictions in order to estimate the error involved with ideal gas approximations.
- e. The wall heat flux was computed for a range of flow conditions in order to obtain a correlation between the Nusselt number and the Reynolds number. The computed relationship was compared with standard correlations for wall heat transfer.
- f. A series of parametric simulations were performed with different gravity vectors to analyze the effect of natural convection. This study was used to obtain the most optimum orientation for the test cell in order to eliminate flow instabilities generated by buoyancy.
- g. A 3-D model was used to simulate the flow pattern and supercritical transport inside the experimental test cell. The results of the simulations were compared with experimental data.
- h. A preliminary work plan for Phase II was prepared.

The details of each of these tasks are discussed in the following sections.

1.4 Outline of the Report

The next section (Section 2) outlines the detailed formulation of the supercritical model. Section 3 presents the computation of properties for SF_6 at various temperatures using the model. Computations for supercritical heat transfer in a 2-D channel are also presented. Section 4 presents the results of 2-D simulations made to estimate the effects of natural convection on the flow patterns inside the test cell. Section 5 describes the experimental setup and apparatus and the data obtained from the experiments. Section 6 presents the results of 3-D simulations of the test cell and comparisons with data. The conclusions from this study and recommendations for future work are discussed in Section 7.

2. FORMULATION OF SUPERCRITICAL TRANSPORT MODEL

This section presents the formulation of models to calculate the variation of properties (such as viscosity, conductivity, density, specific heat, *etc.*) in the critical and supercritical regimes.

2.1 Governing Equations

The mass conservation for the flow can be represented by the continuity equation. This formulation accounts for a variable density flowfield:

$$\frac{\partial \rho}{\partial t} + \nabla \cdot \rho \mathbf{u} = 0.0 \quad (2.1)$$

where ρ is the density of the fluid and \mathbf{u} is the velocity vector.

The momentum conservation equation for the flow is written as:

$$\frac{\partial \rho \mathbf{u}}{\partial t} + \nabla \cdot \rho \mathbf{u} \mathbf{u} = -\nabla p + \nabla \cdot \eta (\nabla \mathbf{u} + \nabla \mathbf{u}^T) + \rho \mathbf{g} \quad (2.2)$$

where η is the viscosity and \mathbf{g} is the gravity vector. It is assumed that the gas behaves as a Newtonian fluid. The energy conservation equation for a single component system (assuming low Mach number and neglecting dissipation) is given by:

$$\rho C_p \left(\frac{\partial T}{\partial t} + \mathbf{u} \cdot \nabla T \right) = \nabla \cdot (\lambda \nabla T) \quad (2.3)$$

where C_p , λ and T are the specific heat, thermal conductivity, and temperature of the fluid, respectively.

The properties such as ρ , η , λ , and C_p in the above equations have to be calculated for the supercritical regime. Ideal gas approximations are not valid due to steep variations (in these properties) across the critical point. The following sections present a detailed formulation for the estimation of supercritical properties.

2.2 Calculation of Viscosity

The low pressure viscosity is calculated from the expression by Chung, *et al*²,

$$\eta = 40.785 \frac{F_c (MT)^{1/2}}{V_c^{2/3} \Omega_v} \quad (2.4)$$

η = viscosity, μP

M = Molecular Weight, g/mol

T = Temperature, $^{\circ}K$

V_c = critical volume, cm^3/mol

Ω_v is a collision integral of the form:

$$\Omega_v = [A(T^*)^{-B}] + C[\exp(-DT^*)] + E[\exp(-FT^*)] \quad (2.5)$$

where

$T^* = kT/\epsilon$, $A = 1.16145$, $B = 0.14874$

$C = 0.52487$, $D = 0.77320$, $E = 2.16178$, $F = 2.43787$

k = Boltzmann Constant

ϵ = characteristic energy of interaction between molecules

The collision integral is based on a Lennard-Jones potential function of the form,

$$\psi(r) = 4\epsilon \left[\left(\frac{\sigma}{r} \right)^{12} - \left(\frac{\sigma}{r} \right)^6 \right] \quad (2.6)$$

where σ is the collision diameter of the molecule.

The factor ε/k can be expressed as:

$$\frac{\varepsilon}{k} = \frac{T_c}{1.2593} \quad (2.7)$$

where T_c is the critical temperature. Therefore,

$$T^* = 1.2593 T_r \quad (2.8)$$

where $T_r = T/T_c$ is the reduced temperature.

The factor F_c is calculated as

$$F_c = 1 - 0.2756 \omega + 0.059035 \mu_r^4 + k \quad (2.9)$$

where ω is an acentric factor dependent on the polarity of the molecule, μ_r is a dimensionless dipole moment and k is a correction for highly polar molecules.

The high pressure viscosity using the Chung formulation is given by:

$$\eta = \eta^* \frac{36.344 (MT_c)^{1/2}}{V_c^{2/3}} \quad (2.10)$$

where

$$\eta^* = \frac{(T^*)^{1/2}}{\Omega_\eta} \left\{ F_c \left[(G_2)^{-1} + E_6 y \right] \right\} + \eta^{**}$$

$$y = \frac{V_c}{6V}; \quad V = \text{molar volume (cm}^3/\text{mol)}$$

$$G_1 = \frac{1 - 0.5 y}{(1 - y)^3}$$

$$G_2 = \frac{E_1 \left\{ \left[1 - \exp(-E_4 y) \right] / y \right\} + E_2 G_1 \exp(E_5 y) + E_3 G_1}{E_1 E_4 + E_2 + E_3}$$

$$\eta^{**} = E_7 y^2 G_2 \exp \left[E_8 + E_9 (T^*)^{-1} + E_{10} (T^*)^{-2} \right]$$

The constants E_1 through E_{10} are tabulated in the following table.

Table 2-1. Constants for the Viscosity Model

$E_i = a_i + b_i w + c_i \mu_r^4 + d_i k$				
i	a_i	b_i	c_i	d_i
1	6.234	50.412	-51.680	1189.0
2	1.210×10^{-3}	-1.154×10^{-3}	-6.257×10^{-3}	0.03728
3	5.283	254.209	-168.48	3898.0
4	6.623	38.096	-8.464	31.42
5	19.745	7.630	-14.354	31.53
6	-1.900	-12.537	4.985	-18.15
7	24.275	3.450	-11.291	69.35
8	0.7972	1.117	0.01235	-4.117
9	-0.2382	0.06770	-0.8163	4.025
10	0.06863	0.3479	0.5926	-0.727

4240/1 11

The above formulation for calculating dense fluid viscosities shows good agreement with experimental data and the errors are usually less than 5%.

2.3 Calculation of Thermal Conductivity

The high pressure thermal conductivity of a substance is given by the expression of Chung *et al*²

$$\lambda = \frac{31.2\eta^0\Psi}{M'} (G_2^{-1} + B_6 y) + q B_7 y^2 T_r^{1/2} G_2 \quad (2.11)$$

λ = thermal conductivity , W/(m-°K)

η^0 = Low pressure gas viscosity, N · S/m²

M' = Molecular weight, kg/mol

$$q = 3.586 \times 10^{-3} \left(T_c / M' \right)^{1/2} / V_c^{2/3}$$

The factor Ψ is given as:

$$\Psi = 1 + \alpha \left\{ [0.215 + 0.28288\alpha - 1.061\beta + 0.26665Z] / [0.6366 + \beta Z + 1.061\alpha\beta] \right\} \quad (2.12)$$

where

$$\alpha = \frac{C_v}{R} - \frac{3}{2}$$

$$\beta = 0.7862 - 0.7109\omega + 1.3168\omega^2$$

$$z = 2.0 + 10.5 T_r^2$$

C_v = Specific heat at constant volume

R = Universal gas constant

$$G_1 = \frac{1 - 0.5y}{(1 - y)^3}$$

$$G_2 = \frac{\left(\frac{B_1}{y}\right) [1 - \exp(-B_4 y)] + B_2 G_1 \exp(B_5 y) + B_3 G_1}{B_1 B_4 + B_2 + B_3}$$

the coefficients B_1 to B_7 are tabulated below.

Table 2-2. Constants for the Thermal Conductivity Model

$$B_i = a_i + b_i \omega + c_i \mu_r^4 + d_i k$$

i	a_i	b_i	c_i	d_i
1	2.4166 E+0	7.4824 E-1	-9.1858 E-1	1.2172 E+2
2	-5.0924 E-1	-1.5094 E+0	-4.9991 E+1	6.9983 E+1
3	6.6107 E+0	5.6207 E+0	6.4760 E+1	2.7039 E+1
4	1.4543 E+1	-8.9139 E+0	-5.6379 E+1	7.4344 E+1
5	7.9274 E-1	8.2019 E-1	-6.9369 E-1	6.3173 E+1
6	-5.8634 E+0	1.2801 E+1	9.5893 E+0	6.5529 E+1
7	9.1089 E+1	1.2811 E+2	-5.4217 E+1	5.2381 E+2

4240/1 12

2.4 Calculation of Density

The Corresponding States principle is used to calculate the density of the fluid,

$$Z = \frac{PV}{RT} \quad (2.13)$$

where Z is the compressibility factor. Z is obtained as:

$$Z = Z^{(0)}(T_r, P_r) + \omega Z^{(1)}(T_r, P_r) \quad (2.14)$$

The function $Z^{(0)}$ would apply to spherical molecules and $Z^{(1)}$ is a deviation function. $Z^{(0)}$ and $Z^{(1)}$ are tabulated as a function of T_r and P_r in Tables 3-2 and 3-3 of Reference 2, respectively.

2.5 Calculation of Enthalpy

For a pure substance,

$$dh = Tds + v dp \quad (2.15)$$

where

h = enthalpy

s = entropy

v = specific volume

Also,

$$ds = \frac{C_p dT}{T} - \left(\frac{\partial v}{\partial T} \right)_p dp \quad (2.16)$$

where

C_p = Specific heat at constant pressure

Substituting Equation (2.15) in Equation (2.16),

$$dh = C_p dT + \left[v - T \left(\frac{\partial v}{\partial T} \right)_p \right] dp \quad (2.17)$$

The enthalpy change at constant temperature is given as:

$$dh_T = \left[v - T \left(\frac{\partial v}{\partial T} \right)_p \right] dp \quad (2.18)$$

Substituting $v = \frac{ZRT}{p}$ we get

$$\begin{aligned}
 dh_T &= \frac{-RT^2}{p} \left(\frac{\partial Z}{\partial T} \right)_p dp \\
 &= -RT_c T_r^2 \left(\frac{\partial Z}{\partial T_r} \right)_{p_r} d \ln p_r
 \end{aligned}$$

$$\frac{h^* - h}{RT_c} = \int_0^p T_r^2 \left(\frac{\partial Z}{\partial T_r} \right)_{p_r} d \ln p_r \quad (2.19)$$

The zero limit for pressure signifies the enthalpy of an ideal gas, h^* . The real gas enthalpy ' h ' at any temperature can be obtained from the above relationship. The RHS of Equation (2.19) is a function of T_r and P_r , i.e.

$$\frac{h^* - h}{RT_c} = F^{(0)} + \omega F^{(1)} \quad (2.20)$$

where $F^{(0)}$ and $F^{(1)}$ are tabulated as functions of T_r and P_r in Tables 5-2 and 5-3 of Reference 2, respectively. The ideal gas enthalpy h^* is obtained from the JANNAF data.

It is observed that the dependence of ' h ' on the temperature is highly non-linear. An iterative process is adopted to obtain the temperature from the enthalpy at any given point in the computational domain.

2.6 Calculation of Specific Heat

Similar to enthalpy, the specific heat can be expressed as:

$$C_p - C_p^* = (\Delta C_p)^{(0)} + \omega (\Delta C_p)^{(1)} \quad (2.21)$$

where C_p^* is the ideal gas specific heat. C_p^* can be calculated from JANNAF data. $(\Delta C_p^*)^{(0)}$ and $(\Delta C_p^*)^{(1)}$ are tabulated in Tables 5-8 and 5-9 of Reference 2, respectively.

3. COMPUTATION OF SUPERCRITICAL TRANSPORT FOR SF₆

Sulfur Hexafluoride (SF₆) was selected as the surrogate fuel for the Phase I simulations and experiments. SF₆ is non-toxic and non-flammable, and can be easily stored as a liquid. On heating, it is a very stable compound with inert behavior similar to nitrogen. Also, its critical state can be achieved easily in the laboratory. This makes SF₆ very suitable for the preliminary experiments.

The critical properties for SF₆ are :

$$T_c = 318.7^\circ\text{K}$$

$$P_c = 37.6 \text{ bars}$$

$$\rho_c = 734.7 \text{ kg/m}^3$$

$$Z_c = 0.282$$

The acentric factor for SF₆ is $\omega = 0.286$ and the molecular weight of SF₆ is 146.05 kg/mol.

3.1 Property Variation with Temperature

The property calculations were done at the critical pressure of 37.6 bars. Figure 3-1 shows the density variation with temperature. It is observed that the density decreases by a factor of 3 across the critical point. The symbols represent data for SF₆¹ in the subcritical regime. Reliable data are not available in the critical and supercritical regimes. The comparison shows that the model is able to predict the density and its variation reasonably well in the subcritical regime. Figure 3-2 shows the dynamic viscosity variation with temperature. A steep decrease in viscosity is observed near the critical point. This correlates well with other observations.^{1,4,5} The thermal conductivity and specific heat variations are shown in Figures 3-3 and 3-4, respectively. It is observed that both quantities have peaks in the vicinity of the critical point. Recent investigations⁵ have reported this unusual behavior for the conductivity and specific heat.

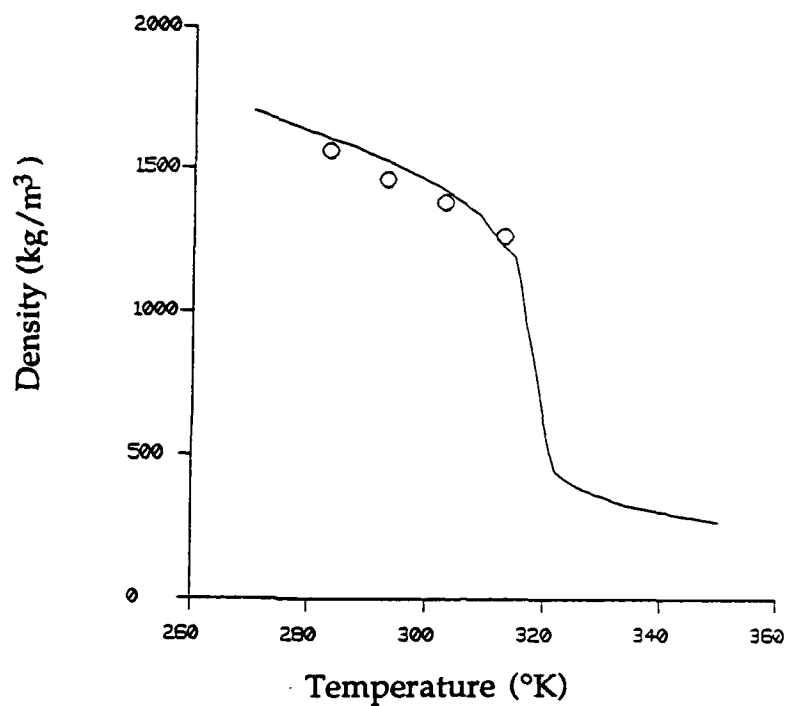


Figure 3-1. Variation of Density with Temperature. Symbols represent data from Reference 1

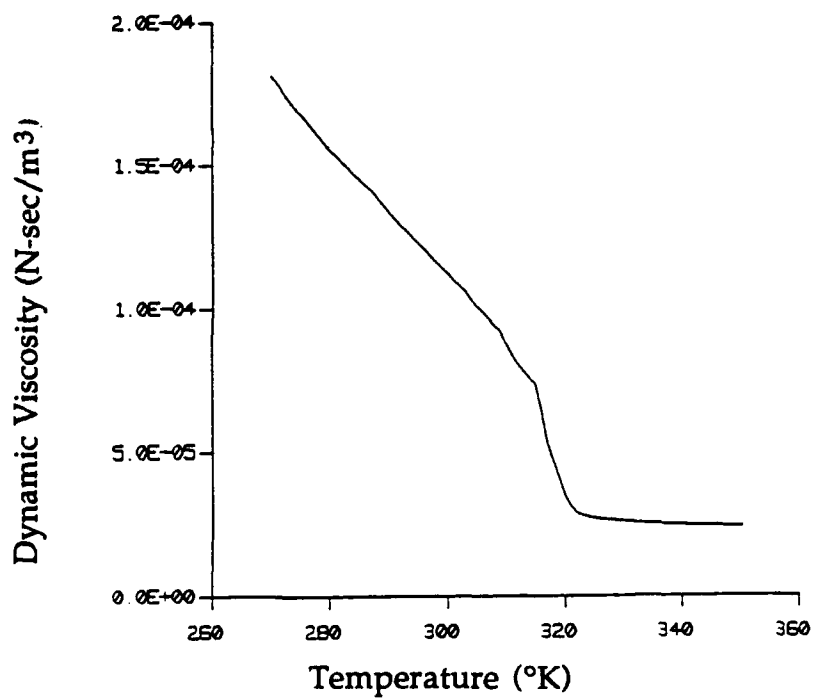


Figure 3-2. Variation of Dynamic Viscosity with Temperature

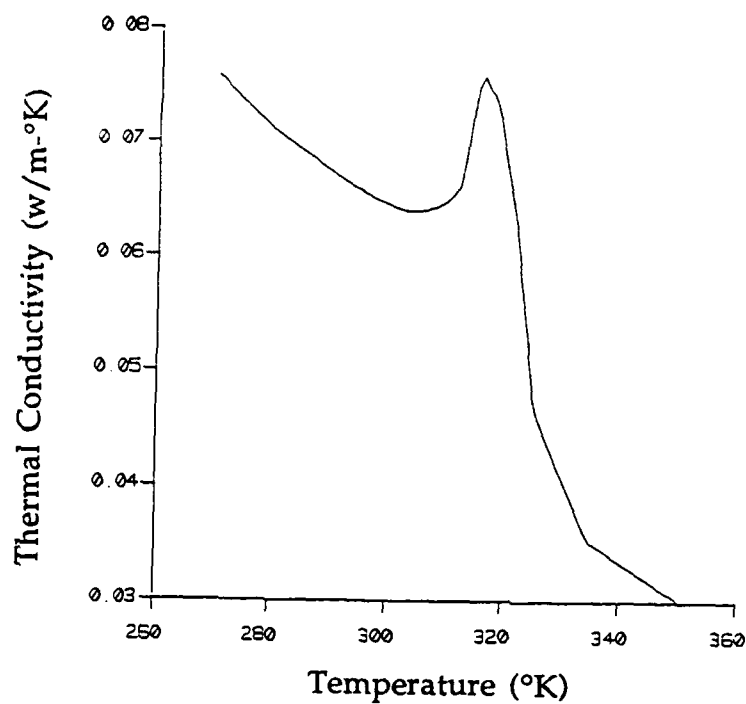


Figure 3-3. Variation of Thermal Conductivity with Temperature

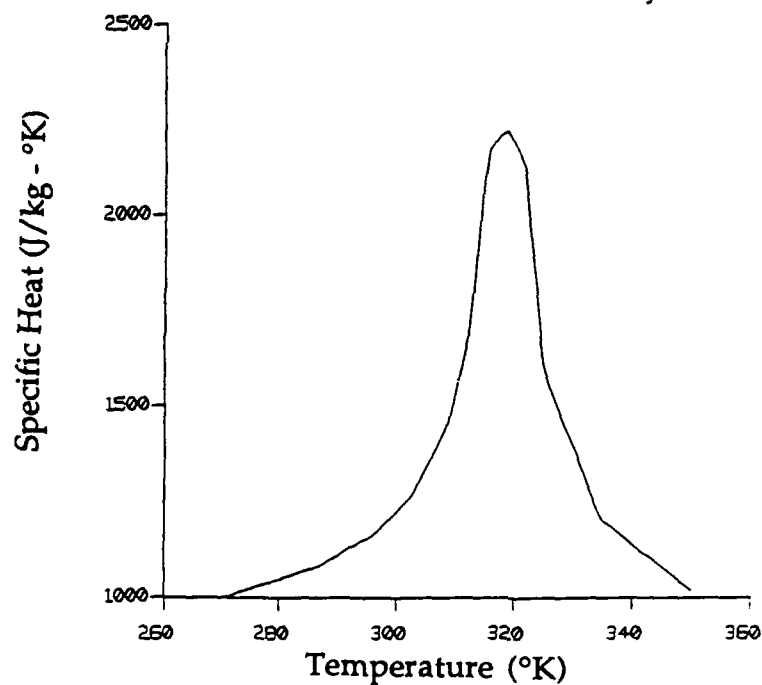


Figure 3-4. Variation of Specific Heat with Temperature

3.2 Supercritical Heat Transfer in a 2-D Channel

Numerical simulations were performed to calculate supercritical heat transfer in a two-dimensional, rectangular channel. The schematic of the channel is shown in Figure 3-5a. The dimensions of the channel correspond with those of the test cell used in the experiments. The flow enters at a subcritical temperature of 300°K with a velocity of 1.16 mm/sec (15cc/min). The bottom wall is maintained at a supercritical temperature of 323°K. Therefore, the wall heating causes the fluid to become critical as it flows along the wall. The computational grid (100 x 50) is shown in Figure 3-5b.

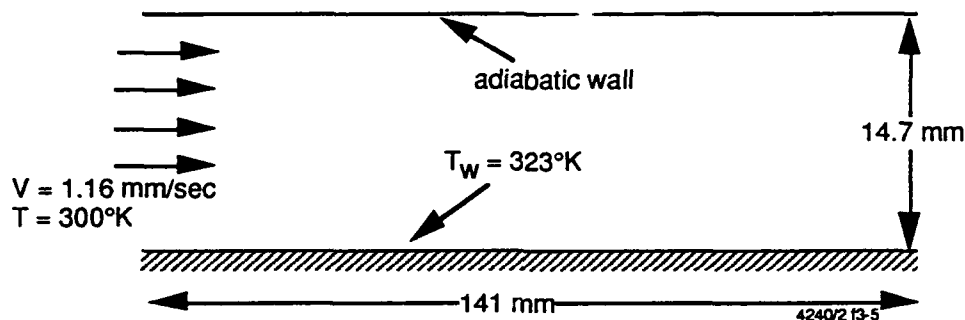


Figure 3-5a. Schematic of the Channel

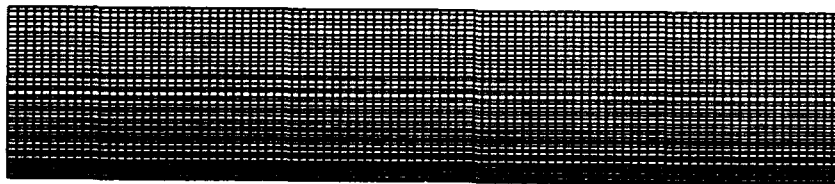


Figure 3-5b. Computational Grid (100 x 50) for the Channel

Figure 3-6 shows the temperature distribution in the channel. Figure 3-7 shows the density distribution in the channel. It is observed that the density decreases sharply near the wall due to fluid becoming supercritical. The heat flux was computed along the wall and is shown by curve 1 in Figure 3-8. The heat flux is large at the leading edge of the wall (due to thinner boundary layers at the leading edge).

```

TEMP  CONTOURS
FMIN  3.000E+02
FMAX  3.228E+02
CONTOUR LEVELS
1      3.000E+02
2      3.012E+02
3      3.024E+02
4      3.036E+02
5      3.048E+02
6      3.060E+02
7      3.072E+02
8      3.084E+02
9      3.096E+02
10     3.108E+02
11     3.120E+02
12     3.132E+02
13     3.144E+02
14     3.156E+02
15     3.168E+02
16     3.180E+02
17     3.192E+02
18     3.204E+02
19     3.216E+02
20     3.228E+02
OK>

```



Figure 3-6. Temperature Distribution (°K) in the Channel

```

RHO  CONTOURS
FMIN  4.316E+02
FMAX  1.454E+03
CONTOUR LEVELS
1      4.316E+02
2      4.854E+02
3      5.392E+02
4      5.930E+02
5      6.468E+02
6      7.007E+02
7      7.545E+02
8      8.083E+02
9      8.621E+02
10     9.159E+02
11     9.697E+02
12     1.024E+03
13     1.077E+03
14     1.131E+03
15     1.185E+03
16     1.239E+03
17     1.293E+03
18     1.346E+03
19     1.400E+03
20     1.454E+03
OK>

```



Figure 3-7. Density (kg/m³) Distribution in the Channel

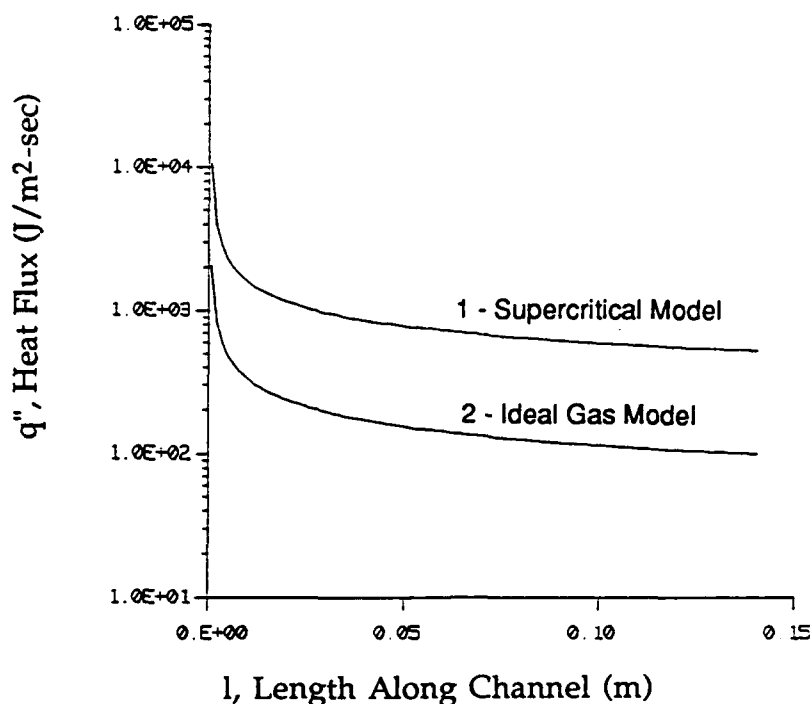


Figure 3-8. Heat Flux Along the Wall of the Channel: Curve 1 - Supercritical Model; Curve 2 - Ideal Gas Model

3.3 Comparison with Ideal Gas Model Predictions

An ideal gas model was used to calculate the heat transfer in the 2-D channel in order to estimate the error involved with the ideal gas approximation. The channel pressure was increased to 248 bars in order to ensure that the density of the gas corresponded to the density of the subcritical fluid in the previous case. The velocity is maintained at 1.16 mm/sec so that the mass flow rates through the channel are the same for the ideal gas model and the supercritical model. The computed wall heat flux along the wall from the ideal gas model is shown by curve 2 in Figure 3-8. It is observed that the supercritical model predicts larger heat flux values at the wall for the same boundary conditions. Figure 3-9 shows the density distribution in the channel predicted by the ideal gas model. It is observed that the ideal gas model predicts only a small decrease in density compared to the supercritical model (Figure 3-7).

```

RHO   CONTOUR
FMIN  1  352E+03
FMAX  1  454E+03
CONTOUR LEVELS
1      1  352E+03
2      1  363E+03
3      1  375E+03
4      1  386E+03
5      1  397E+03
6      1  409E+03
7      1  420E+03
8      1  431E+03
9      1  443E+03
10     1  454E+03
OK>

```

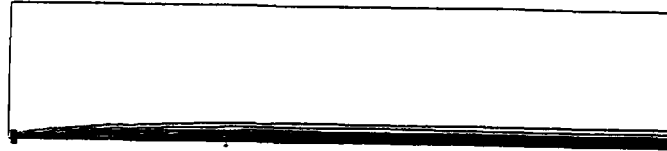


Figure 3-9. Density (kg/m^3) Distribution (with Ideal Gas Model) in the Channel

3.4 Correlation Between Dimensionless Quantities

A series of simulations were performed for different flow rates through a 2-D channel in order to correlate the Nusselt number with the Reynolds number. The schematic of the channel is shown in Figure 3-10. A fully developed velocity profile is assumed at the inlet. The fluid enters at a temperature of 300°K and the walls of the channel are maintained at 323°K . The mean velocity through the channel is used as a parameter to vary the Reynolds number. The computed wall heat flux (for the entire wall) is plotted (curve 1) in Figure 3-11 as a function of the mean velocity. Curve 2 shows the results obtained from the ideal gas approximation.

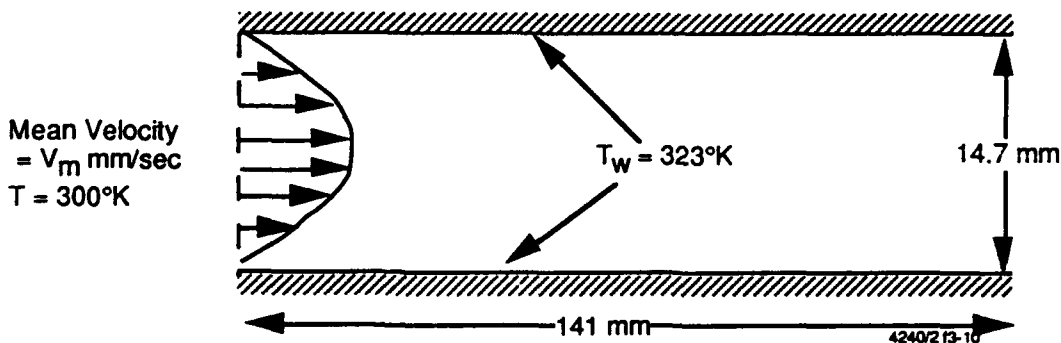


Figure 3-10. Schematic of the Channel and Boundary Conditions

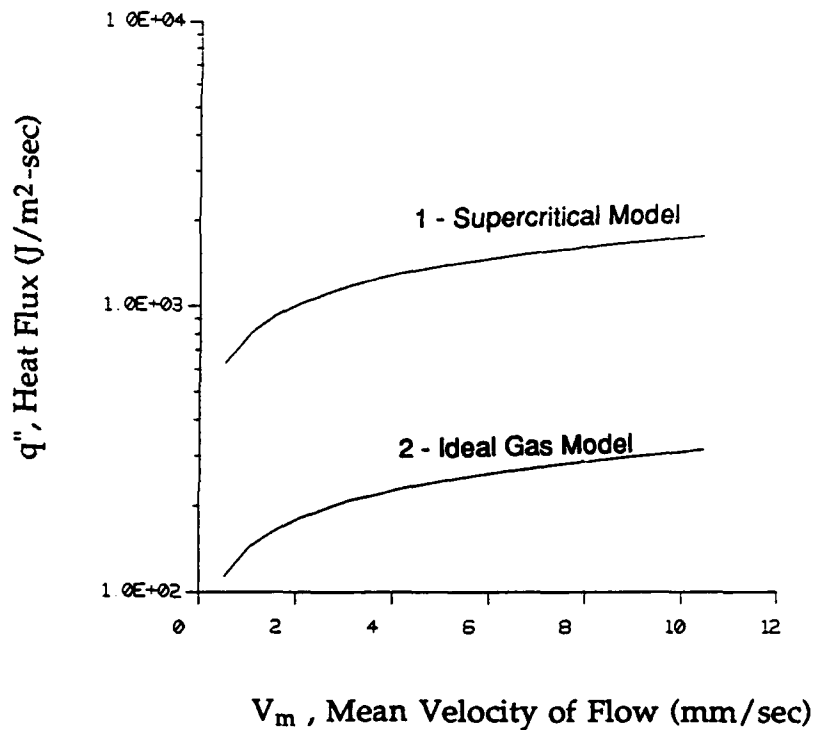


Figure 3-11. Variation of Heat Flux with Mean Velocity Through the Channel.
Curve 1 - Supercritical Model; Curve 2 - Ideal Gas Model

A curve fit of the heat flux values results in the following correlations:

$$\tilde{q}_L = K_1 V_m^{1/3} \quad (3.1)$$

for the supercritical model, and

$$\tilde{q}_L = K_2 V_m^{1/3} \quad (3.2)$$

for the ideal gas model. Where \tilde{q}_L is the heat flux over the length L , V_m is the mean velocity, and K_1 and K_2 are proportionality constants. It is interesting to note that

the supercritical model and the ideal gas model predict the same dependence for heat flux on the mean velocity. However, the proportionality constant, K_1 , for the supercritical model is larger than K_2 , the proportionality constant for the ideal gas model.

The Nusselt number is expressed as:

$$Nu_L = \frac{hL}{\lambda} \quad (3.3)$$

where h is the heat transfer coefficient = $\frac{\dot{q}_L}{\Delta T}$, L is the length of the wall, and λ is the thermal conductivity of the freestream fluid. The Reynolds number is expressed as:

$$Re = \frac{\rho V_m H}{\eta} \quad (3.4)$$

where H is the channel height, and ρ and η are the density and dynamic viscosity of the freestream fluid. Therefore, Equations (3.1) and (3.2) can be rewritten as:

$$Nu_L \propto Re^{1/3} \quad (3.5)$$

The standard correlation for heat transfer in a long duct is expressed as:⁶

$$Nu_L = 1.86 \left(Re \cdot Pr \cdot \frac{H}{L} \right)^{1/3} \left(\frac{\mu_b}{\mu_s} \right)^{0.14} \quad (3.6)$$

where Pr is the Prandtl number, μ_b and μ_s are the dynamic viscosities in the bulk fluid and heated surface, respectively. It is observed that the supercritical model and

the ideal gas model predict correctly the dependence of Nusselt number on the Reynolds number. The proportionality constant for the supercritical model is higher than that of the ideal gas model. From Figure 3-11, it is observed that $K_1 \approx 6K_2$. However, the thermal conductivity predicted by the supercritical model at the heated wall is only 3 times as large as that predicted by the ideal gas model. In order to understand the sixfold increase in heat flux, it is necessary to study the boundary layer profiles in the near wall region. Figure 3-12 shows the velocity profiles (midway in the channel) predicted by the two models. It is observed that the steep decrease in density predicted by the supercritical model causes the fluid near the wall to accelerate leading to a thinner boundary layer (reflected by the larger slope in the profile near the wall). This results in a larger heat flux than what the ratio of conductivities would indicate.

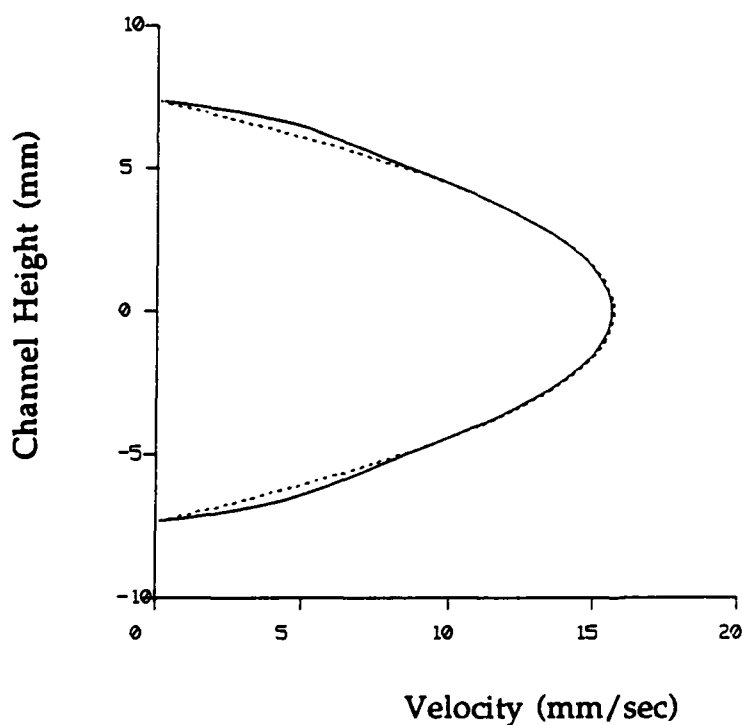


Figure 3-12. Velocity Profile in the Channel. ----- Ideal Gas Model; — Supercritical Model

4. ASSESSMENT OF NATURAL CONVECTION EFFECTS

The results obtained in the previous section show that the density of SF_6 decreases by a factor of 3 across the critical point. This decrease occurs over a temperature interval of 10°K . One of the main concerns in experimenting with supercritical fluids has been the effect of buoyancy which may be quite significant due to the presence of the large density gradient. Buoyancy could introduce gravity driven flow instabilities and thus complicate the study (and hence the understanding) of supercritical transport phenomena. One of the goals of this study was to obtain an appropriate orientation for the test cell that would minimize flow instabilities (especially in the near wall region) due to natural convection. This section presents the results for flow in a 2-D channel (dimensions and boundary conditions are shown in Figure 3-5) with different orientations of the gravity vector.

4.1 Case 1: Gravity Vector $g_y = -9.81 \text{ m/sec}^2$

Figure 4-1 shows the pressure distribution in the channel. The pressure increases in the negative y-direction due to the hydrostatic pressure gradient. Figure 4-2 shows the streamlines for this case. It is observed that the pressure gradient interacts with the density gradient near the wall to produce gravity driven recirculation zones (*i.e.*, flow separation from the wall) in the channel. Figure 4-3 shows the heat flux distribution along the channel wall. The recirculating flow results in a highly non-smooth distribution of heat flux along the channel. The result from the zero gravity case is shown as a dashed line.

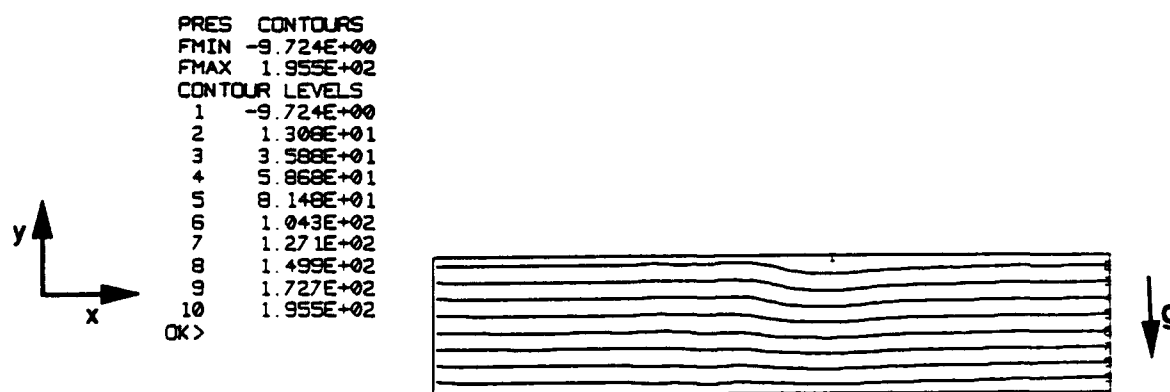


Figure 4-1. Pressure Distribution (Pascals) in the Channel for Case 1

```

STRM CONTOURS
FMIN -7.703E-01
FMAX 2.606E-01
CONTOUR LEVELS
1 -7.703E-01
2 -7.161E-01
3 -6.618E-01
4 -6.076E-01
5 -5.533E-01
6 -4.990E-01
7 -4.448E-01
8 -3.905E-01
9 -3.363E-01
10 -2.820E-01
11 -2.277E-01
12 -1.735E-01
13 -1.192E-01
14 -6.498E-02
15 -1.072E-02
16 4.354E-02
17 9.780E-02
18 1.521E-01
19 2.063E-01
20 2.606E-01
OK>

```

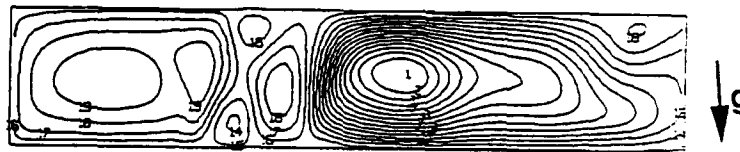


Figure 4-2. Streamline Contours for Case 1

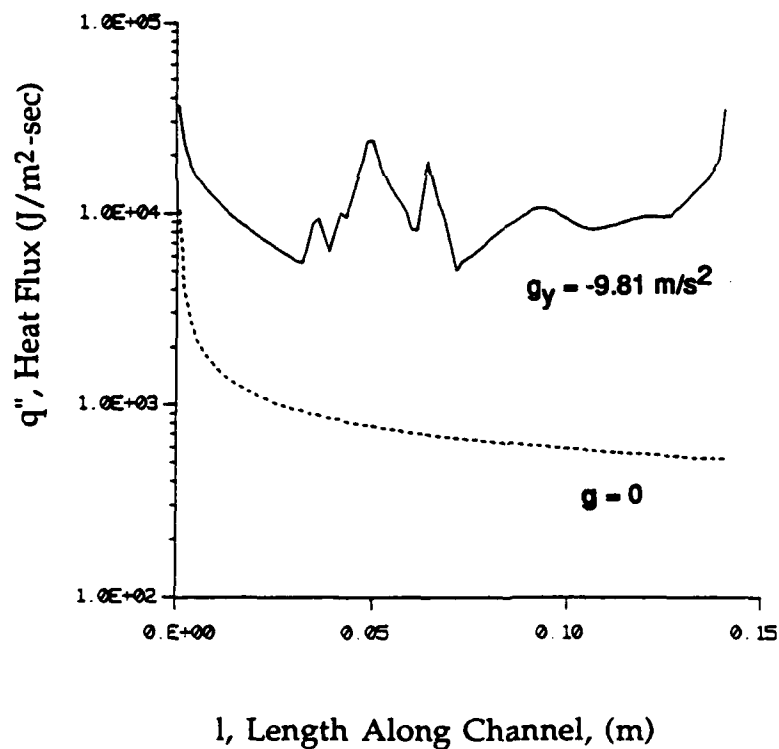


Figure 4-3. Heat Flux Along the Channel Wall. — Results for Case 1; ---- Results with Zero Gravity

4.2 Case 2 : Gravity Vector $g_y = 9.81 \text{ m/sec}^2$

The direction of the hydrostatic pressure gradient is reversed as compared to the previous case. Figures 4-4 and 4-5 show the pressure distribution and the streamlines in the channel respectively. Again, flow instabilities due to buoyancy are observed in the channel. The effect of the instabilities are reflected in the heat flux curve shown in Figure 4-6.

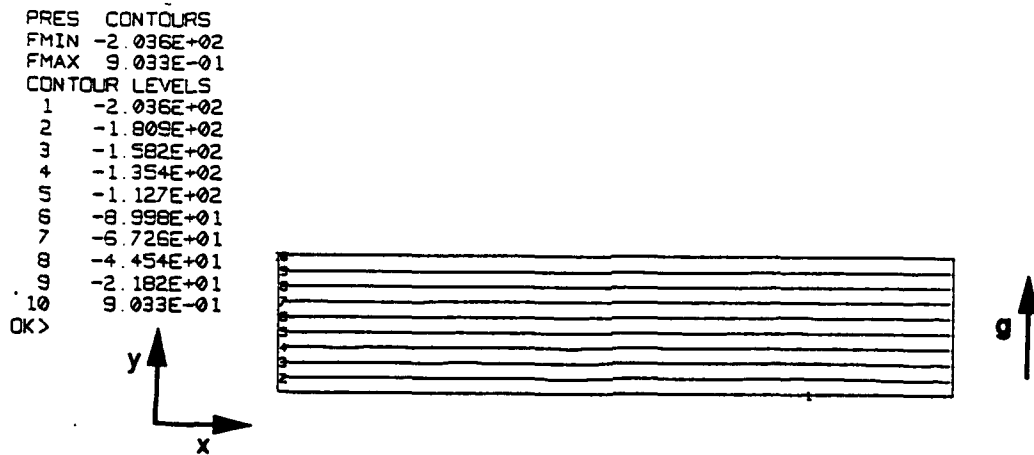


Figure 4-4. Pressure Distribution (Pascals) for Case 2

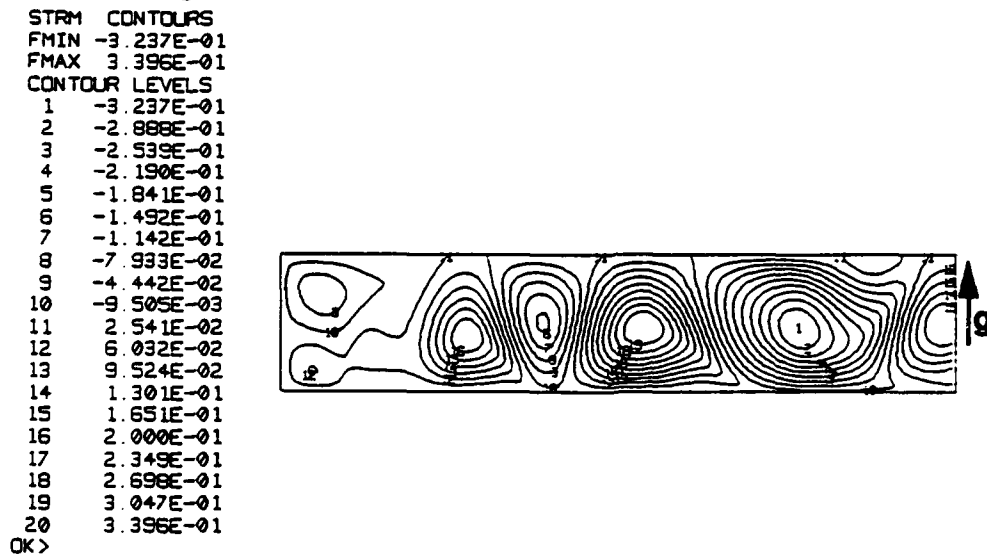


Figure 4-5. Streamline Contours for Case 2

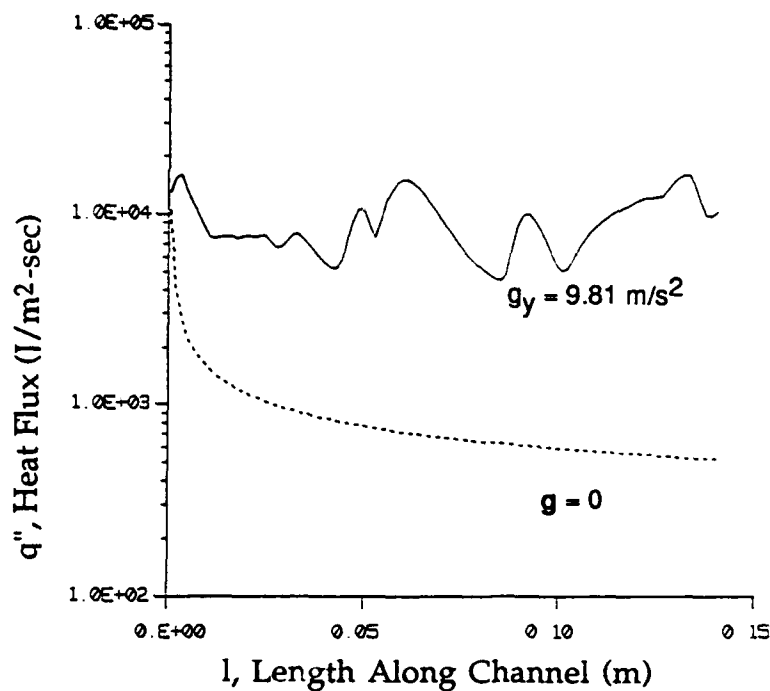


Figure 4-6. Heat Flux Along the Channel Wall. — Results for Case 2;
 --- Results with Zero Gravity

4.3 Case 3: Gravity Vector $g_x = 9.81 \text{ m/sec}^2$

The gravity vector now points in the positive x-direction, *i.e.*, the channel is vertical with the flow going from top to bottom. Figure 4-7 shows the pressure distribution in the channel. The streamlines shown in Figure 4-8 indicate the presence of buoyancy driven cells. Figure 4-9 shows the heat flux distribution along the channel.

```
PRES CONTOURS
FMIN -1.778E+03
FMAX -1.016E+01
CONTOUR LEVELS
1 -1.778E+03
2 -1.685E+03
3 -1.591E+03
4 -1.496E+03
5 -1.405E+03
6 -1.312E+03
7 -1.219E+03
8 -1.126E+03
9 -1.033E+03
10 -9.404E+02
11 -8.473E+02
12 -7.543E+02
13 -6.613E+02
14 -5.683E+02
15 -4.753E+02
16 -3.822E+02
17 -2.892E+02
18 -1.962E+02
19 -1.032E+02
20 -1.016E+01
OK>
```

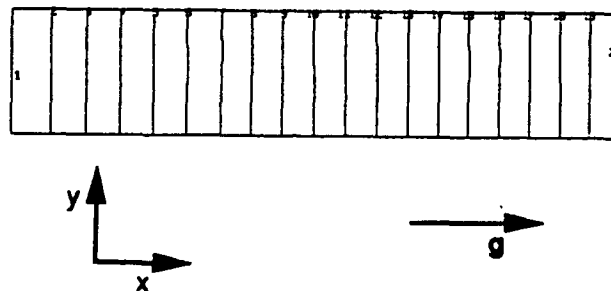


Figure 4-7. Pressure Distribution (Pascals) for Case 3

```

STRM  CONTOURS
FMIN  -5.698E-01
FMAX   5.301E-01
CONTOUR LEVELS
1      -5.698E-01
2      -5.115E-01
3      -4.540E-01
4      -3.961E-01
5      -3.382E-01
6      -2.803E-01
7      -2.225E-01
8      -1.646E-01
9      -1.067E-01
10     -4.879E-02
11     9.095E-03
12     6.698E-02
13     1.249E-01
14     1.828E-01
15     2.406E-01
16     2.985E-01
17     3.564E-01
18     4.143E-01
19     4.722E-01
20     5.301E-01
OK>

```

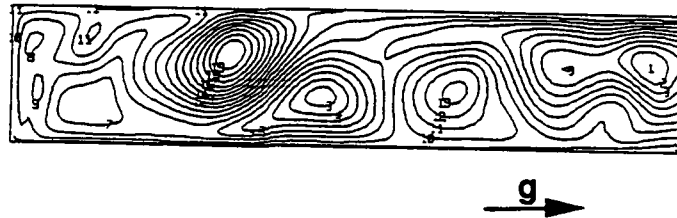


Figure 4-8. Streamline Contours for Case 3

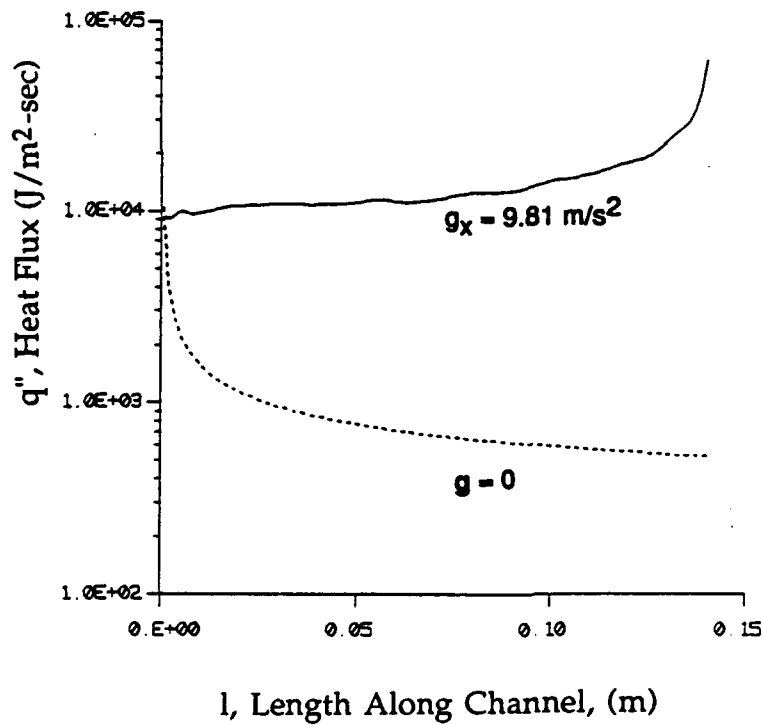


Figure 4-9. Heat Flux Along the Channel Wall. — Results for Case 3; ---- Results with Zero Gravity

4.4 Case 4 : Gravity Vector $g_x = -9.81 \text{ m/sec}^2$

The gravity vector is in the negative x-direction, *i.e.*, the channel is vertical with the flow going from the bottom to the top. Figure 4-10 shows the pressure distribution in the channel. The streamlines in Figure 4-11 indicate a smooth flow pattern (*i.e.*, there is no flow separation). The effect of buoyancy in this orientation is to accelerate the low density fluid near the wall upwards. However, the recirculation zones observed in all the previous cases, are absent. This is also reflected in the smooth nature of the curve for the heat flux distribution (Figure 4-12). The effect of flow acceleration near the wall produces higher values for the heat flux compared to the zero gravity case.

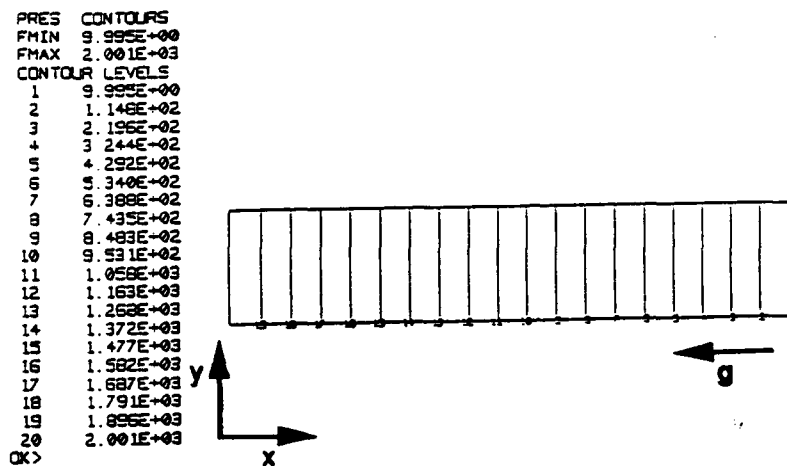


Figure 4-10. Pressure Distribution (Pascals) for Case 4

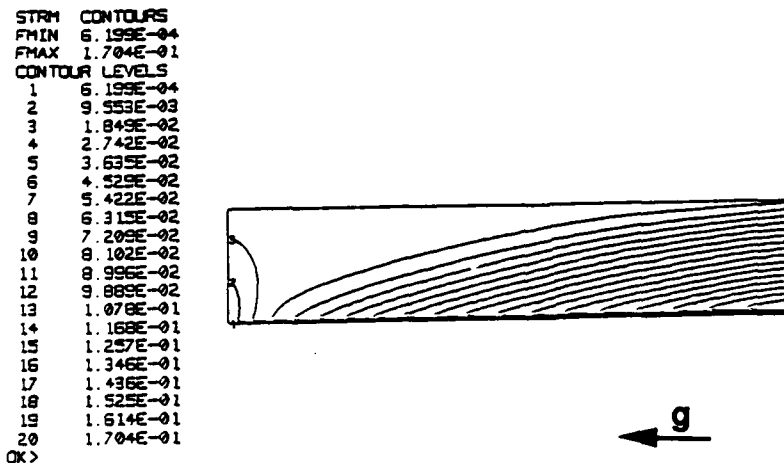


Figure 4-11. Streamline Contours for Case 4

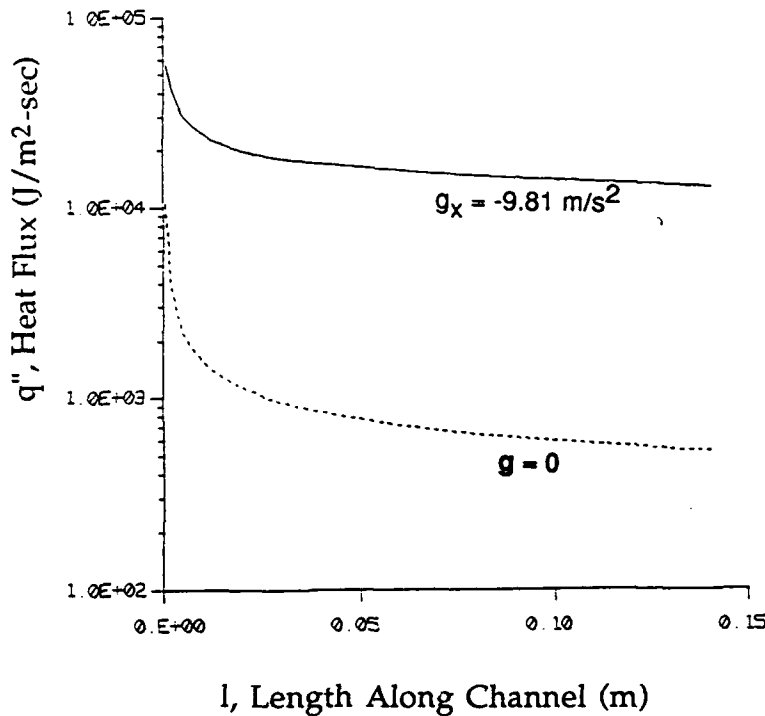


Figure 4-12. Heat Flux Along the Channel Wall. — Results for Case 4; ---- Results with Zero Gravity

From the above simulations, it is clear that the best possible orientation is that corresponding to Case 4, *i.e.*, a vertical channel with flow going from bottom to top. The mean flow patterns for this case are smooth (without flow separation) which result in a smooth heat flux distribution. Again, it should be noted that the effect of gravity in this orientation is to accelerate the low density fluid upwards causing higher rates of heat transfer from (almost an order of magnitude higher) the wall. Figure 4-13 shows the temperature distribution in the channel for case 4. It is observed that the accelerating flow near the wall causes the thermal boundary layer to become very thin.

Based on the above simulations, a vertical orientation (with the flow going from the bottom to the top) was selected. The experiments discussed in the next section were done with this orientation for the test cell.


```
TEMP CONTOURS
FMIN 3.000E+02
FMAX 3.209E+02
CONTOUR LEVELS
1 3.000E+02
2 3.023E+02
3 3.047E+02
4 3.070E+02
5 3.093E+02
6 3.116E+02
7 3.140E+02
8 3.163E+02
9 3.186E+02
10 3.209E+02
OK>
```



Figure 4-13. Temperature Distribution (°K) in the Channel for Case 4

5. EXPERIMENTAL RESULTS FOR SUPERCRITICAL HEAT TRANSFER

This section presents the experimental results obtained at the University of Iowa. SF_6 was used as the simulant fluid and the experiments were performed in the subcritical, critical, and supercritical regimes. The results are shown in the form of shadowgraphs.

5.1 Experimental Apparatus

A square channel with an interior cross section of 15 mm by 15 mm is used for the heat transfer experiments. This square channel is fitted with removable walls. Two optical quality windows are fitted on the opposite sides of the apparatus. One side of the channel wall is fitted with a heater block, and the other side a thermocouple holder block. The viewing area of the optical access is 15 mm by 141 mm. This square channel is the test cell for the heat transfer experiments. The heat transfer test cell is mounted vertically upward on a vibration-isolated optical table. A schematic diagram of the experimental set-up is shown in Figure 5-1. A digitized (video) image of the apparatus is shown in Figure 5-2. The inlet of the test cell is its lower port and the exit is the upper one. The inlet port is plumbed to a feeder cylinder which is essentially a high pressure canister. The interior volume of this canister is 2.5 liters. The feeder cylinder is connected to liquid SF_6 supply and to a high pressure helium cylinder. Liquid SF_6 is supplied to the feeder cylinder by its own vapor pressure. Helium is used to pressurize the liquid SF_6 in the feeder cylinder to desired pressures. A pressure relief valve set at 4.34 MPa (600 psia) is installed in-line between the feeder cylinder and the helium supply, and the other installed in between the feeder cylinder and the test cell. The pressure is measured by a pressure transducer (Omega Model PX302-1KGV) and monitored by a transducer indicator (Omega Model DP-350).

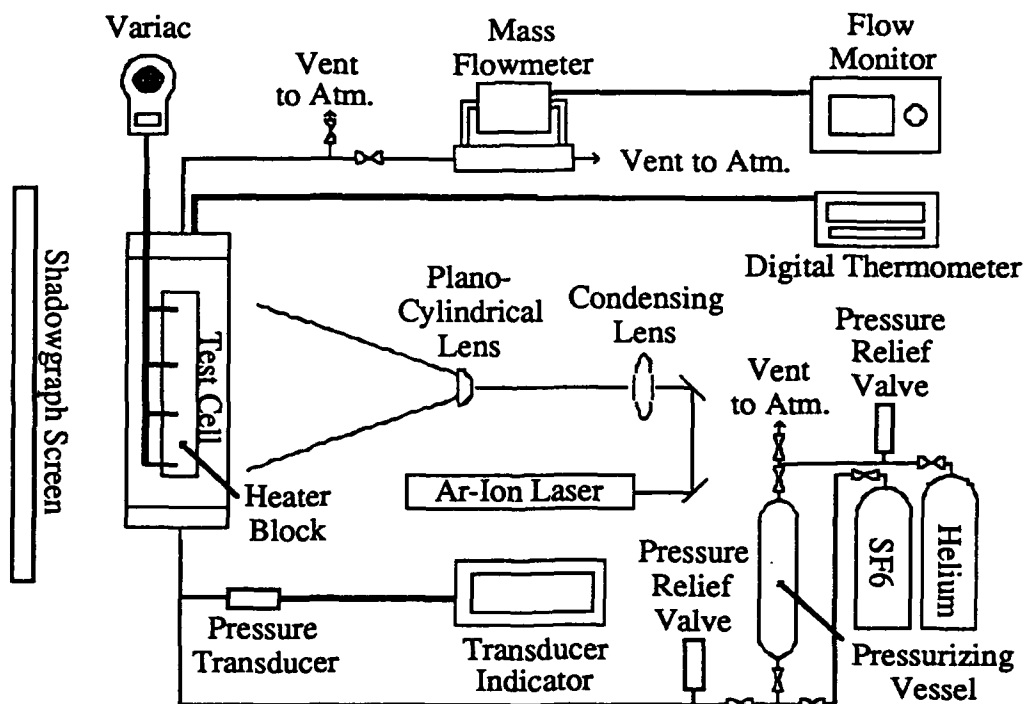


Figure 5-1. Schematic of the Experimental Set-Up

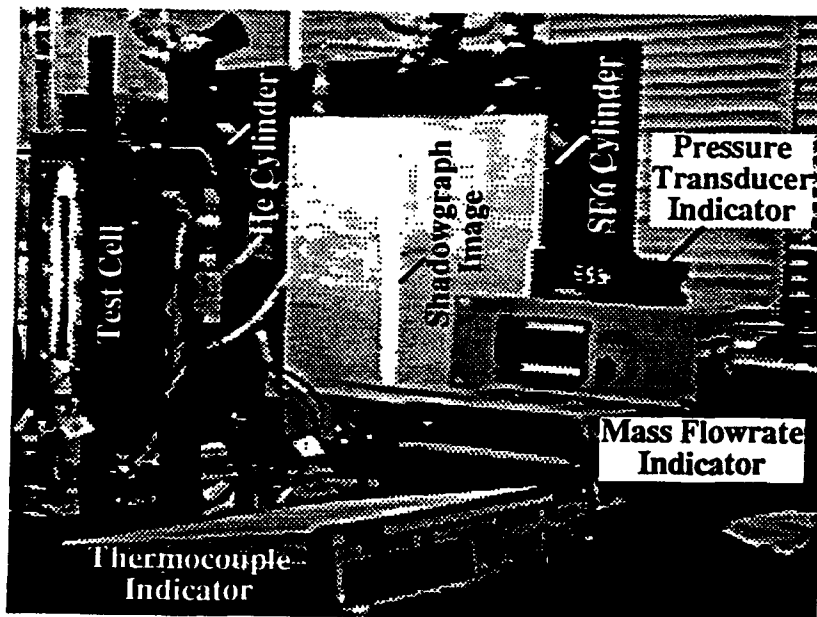


Figure 5-2. Digitized Image of the Apparatus

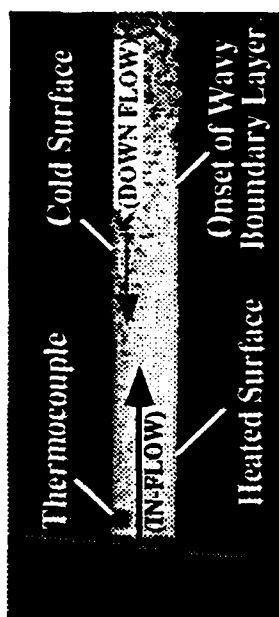
The heater block is electrically heated by using a Variac (Staco Energy Product, Model 3PN1010V). K-type thermocouples are spot-welded onto the heater block to monitor the heater block temperature. The bulk fluid temperature inside the test cell is measured by three sheathed K-type thermocouples; they are respectively located near the inlet, mid-section, and exit of the test cell. These sheathed thermocouples are introduced to the flow through the holder block which is located at the opposite side from the heater block. A thermocouple indicator (Fluke Model 2190A) is used to monitor the temperatures of the heater block and the bulk fluid.

The SF₆ flow rate is regulated by a fine metering valve (Nupro B-4MG), and monitored by a mass flowrate meter (with flow elements of Hastings Model FST and flowrate monitor Hastings Model PR-4AJ). The flow meter was calibrated for air flow rates. The conversion factor was provided by the vendor for SF₆.

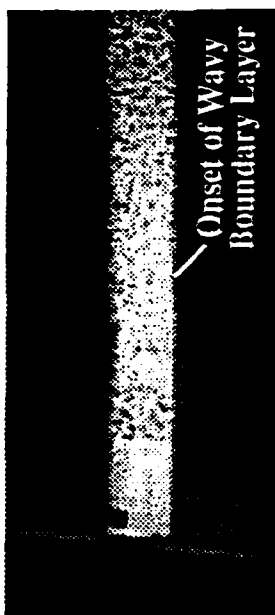
The shadowgraph flow visualization is used for the present study of the transport process. An argon-ion laser (Coherent Model Innova-70) is used as the light source. The optical set-up consists of a condensing lens and a plano-cylindrical lens. The cylindrical lens is used to accommodate the slender rectangular shape of the viewing window. The shadowgraph is projected onto a screen and is recorded by a CCD video camera (Panasonic Model AG-180). A frame grabber (Scion Image Capture II) is used to digitize the video image for review and analysis. A still camera is also used to record some of the shadowgraph images.

5.2 Results and Discussion

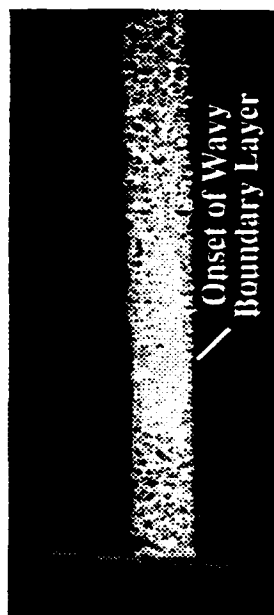
At zero, or low SF₆ flow rates, the heating of SF₆ at a near critical pressure condition with the heater block maintained at the near critical temperature results in recirculation cells in the channel. At a zero flow rate, a stratified region is first formed in the near exit region followed by a gradual down-flow along the cold surface of the unheated sides. This down-flow is a time-dependent phenomenon, and is evident in the video taped images at 16.4 cc/min inlet flow rate, cf., Figure 5-3a. The SF₆ volumetric flowrate is calculated from the mass flow rate with the correction for the compressibility factor difference between the atmospheric condition and the inlet fluid state.



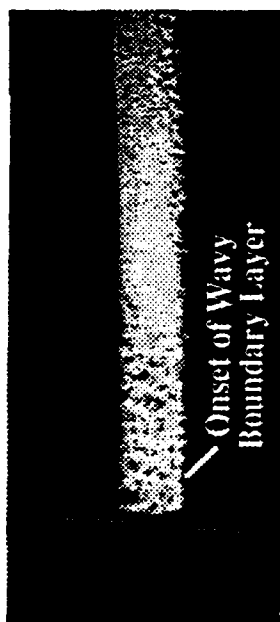
(a)



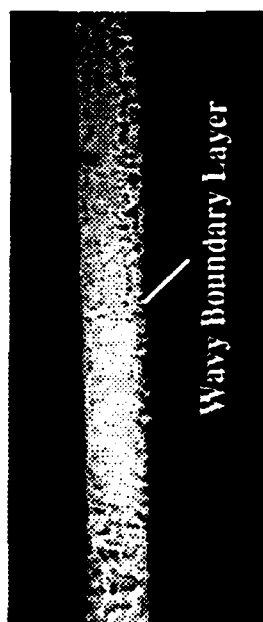
(b)



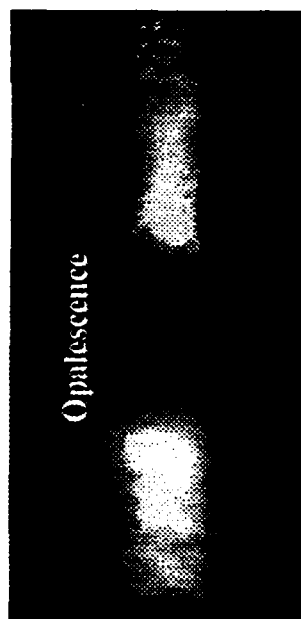
(c)



(d)



(e)



(f)

Figure 5-3. Shadowgraph Images of the Flow in the Test Cell

Vigorous mixing between the fluid adjacent to the heated surface and the "free-stream fluid" is evident from the ejection phenomenon of the fluid parcels (or blobs) from the boundary in the shadowgraph. This ejection of the fluid blobs is similar to the turbulence spots in boundary-layer flows. Figure 5-3a also shows the down flow along the unheated surface. The down flow action is a result of the cooling of the hot SF_6 or the stratified fluid that has accumulated in the upper region of the channel. Without introducing an SF_6 flow, the channel flow becomes a cavity flow with a strong mixing of the fluid inside the channel. When the flow rate is introduced, for example, at 16.4 cc/min of Figure 5-3a, the lower 1/3 region of the field of view shows a "calm flow" region. This "calm flow" region grows in size when the SF_6 flow rate is increased from zero until a limiting condition is reached beyond which its size reduces when the flow rate is increased. This is shown in Figure 5-3b where the flow rate at the inlet is maintained at 35.6 cc/min. At this condition, the onset of the "turbulence spot" in the boundary layer moves toward the channel inlet. With further increase of the SF_6 flow rate, the onset of the wavy boundary layer or the turbulence spots moves toward the channel inlet, for example as shown in Figures 5-3c and 5-3d where the inlet flow rate is maintained at 41.0 and 38.3 cc/min. The system pressure is maintained at $Pr = 1.02$, 1.01, and 0.83 for Figures 5-3b, 5-3c, and 5-3d, respectively; where Pr is the reduced pressure based on the critical pressure of SF_6 . Figure 5-3e shows the turbulence spots develop into a turbulent boundary-layer-like flow shown by the large structures in shadowgraph visualization. It should be noted that the ejection of fluid parcels is also observed along the unheated surface due to the cooling effect. This ejection of the fluid blobs, however, may be an illusion of the collapsing fluid parcels due to decrease of the specific volume when the hot fluid approaches the cold surface. When the heater block is maintained at 40°C ($Tr = 0.98$), and the flow rate maintained at 30.1 cc/min, the heating increases the liquid SF_6 from 21°C at the inlet to 30°C at the top of the heater block.

When the heater block is maintained at a high temperature, *e.g.*, Figure 5-3f, where the mid-section thermocouple registers a temperature of $Tr = 1.02$ and the exit fluid temperature of $Tr = 1.04$, the opalescence, a near critical phenomenon, is seen. Tr is the reduced temperature based on the critical temperature of SF_6 . The opalescence results in a highly distorted image, and a nearly opaque section of Figure 5-3f due to

the large variation of the refractive index due to the fluid approaching the critical point. The flowrate of Figure 5-3f is maintained at 30.1 cc/min. This large variation of the refractive index is evident in the shadowgraph of the near wall fluid structures that shows the refraction of the light beam outside the boundary of the viewing port.

6. 3-D COMPUTATIONS OF SUPERCRITICAL TRANSPORT IN THE TEST CELL

The supercritical models, described in Section 2, were incorporated into a 3-D CFD code. In the experiments, the fluid enters the test cell (square in cross section) through a cylindrical tube. This gives rise to a 3-dimensional flow near the inlet thus necessitating the use of a 3-D model.

6.1 Computational Grid and Boundary Conditions

The schematic of the test cell is shown in Figure 6-1. The flow enters through a circular tube into the rectangular test cell. A fully developed parabolic velocity profile is specified at the inlet to the test cell. A mean velocity of 13 mm/sec (corresponding to a flow rate of 25 l/m) is used as the inlet flow condition. The inlet temperature is 300°K and the bottom wall of the test cell is maintained at 323°K. The test cell pressure is 37.6 bars. The flow, after passing through the test cell, exits into a circular tube. The orientation of the test cell (based on earlier 2-D simulations) is vertical with the flow going from the bottom to the top, *i.e.*, the gravity vector is opposite to the mean flow direction.

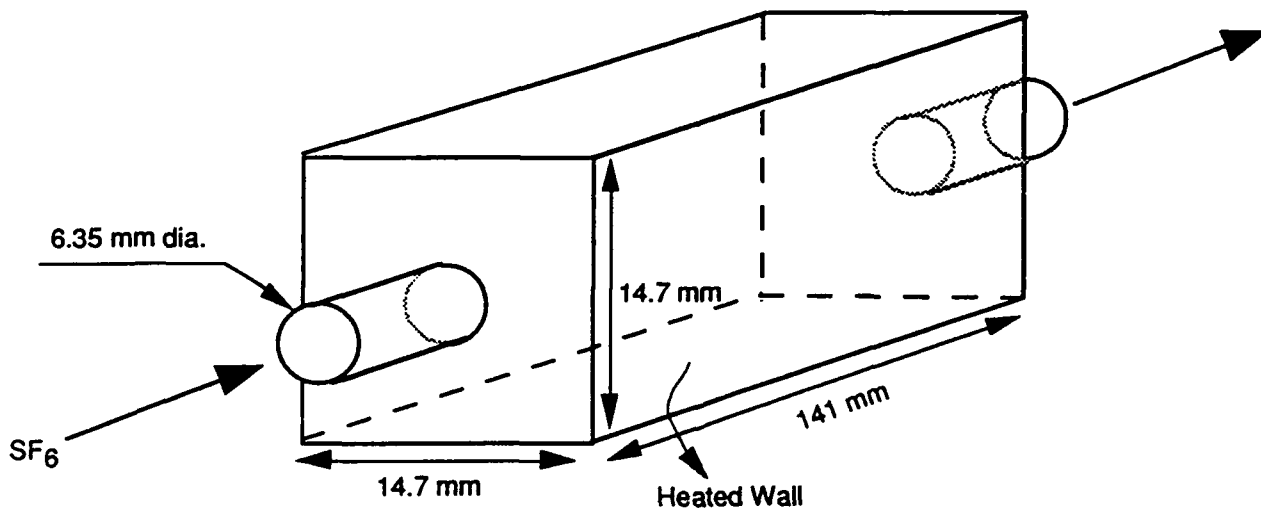


Figure 6-1. Schematic of the Test Cell

The computational grid for the test cell is shown in Figure 6-2. The grid has 61 nodes along the tube, 43 cells in the direction normal to the heated plate, and 44 cells in the transverse plane of the heated plate. The grid is clustered near the heated boundary in order to resolve steep variations in the profiles of the flow properties. A time dependent, 3-D calculation was performed to analyze the transport process within the test cell.

6.2 Results of Numerical Simulations

Figure 6-3 shows the density distribution in the test cell. It is observed that there is a steep variation in density near the heated wall. However, this variation is confined to a very thin layer adjacent to the wall. The velocity vectors, shown in Figure 6-4, indicate the flow acceleration near the heated wall due to buoyancy effects. The accelerating flow causes the boundary layer to become extremely thin. The impingement of this high velocity flow on the rear wall of the test cell results in a recirculation zone near the exit. The computed flow results show a downflow of fluid on the unheated wall. This is also observed in the experiments (Figure 5-3). Figure 6-5 shows the temperature distribution inside the test cell. The increase in temperature is confined to a thin layer adjacent to the wall. However, the recirculation zone near the exit brings the heated fluid from the wall to the core region of the test cell.

Figure 6-6 shows the heat flux distribution on the heated wall of the test cell. The heat flux values are higher at the leading edge of the wall due to thinner boundary layers. However, the general profile of the heat flux distribution is the same as that predicted by the 2-D simulations. Some 3-dimensionalities are observed in the heat flux distribution due to the effect of the velocity profiles.

6.3 Discussion

The major features of the experimental flow field are reproduced by the model. The acceleration of the fluid along the heated wall, the downflow along the unheated wall, and the recirculating flow near the test cell exit are predicted correctly by the simulations.

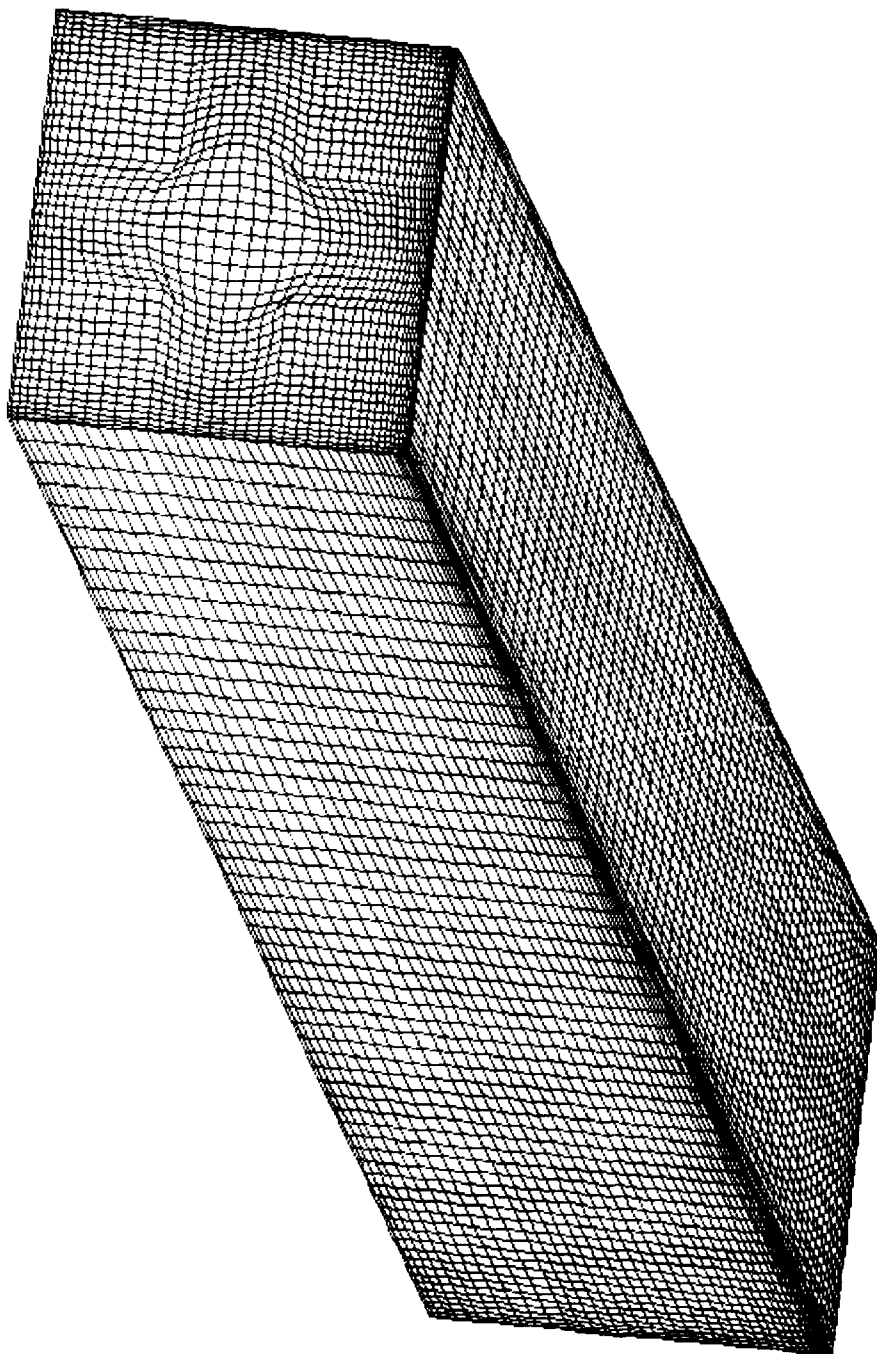


Figure 6-2. Computational Grid for the Test Cell

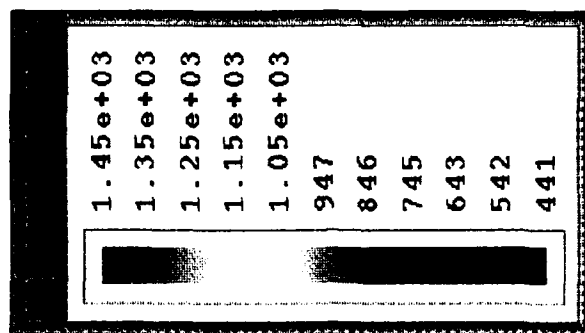
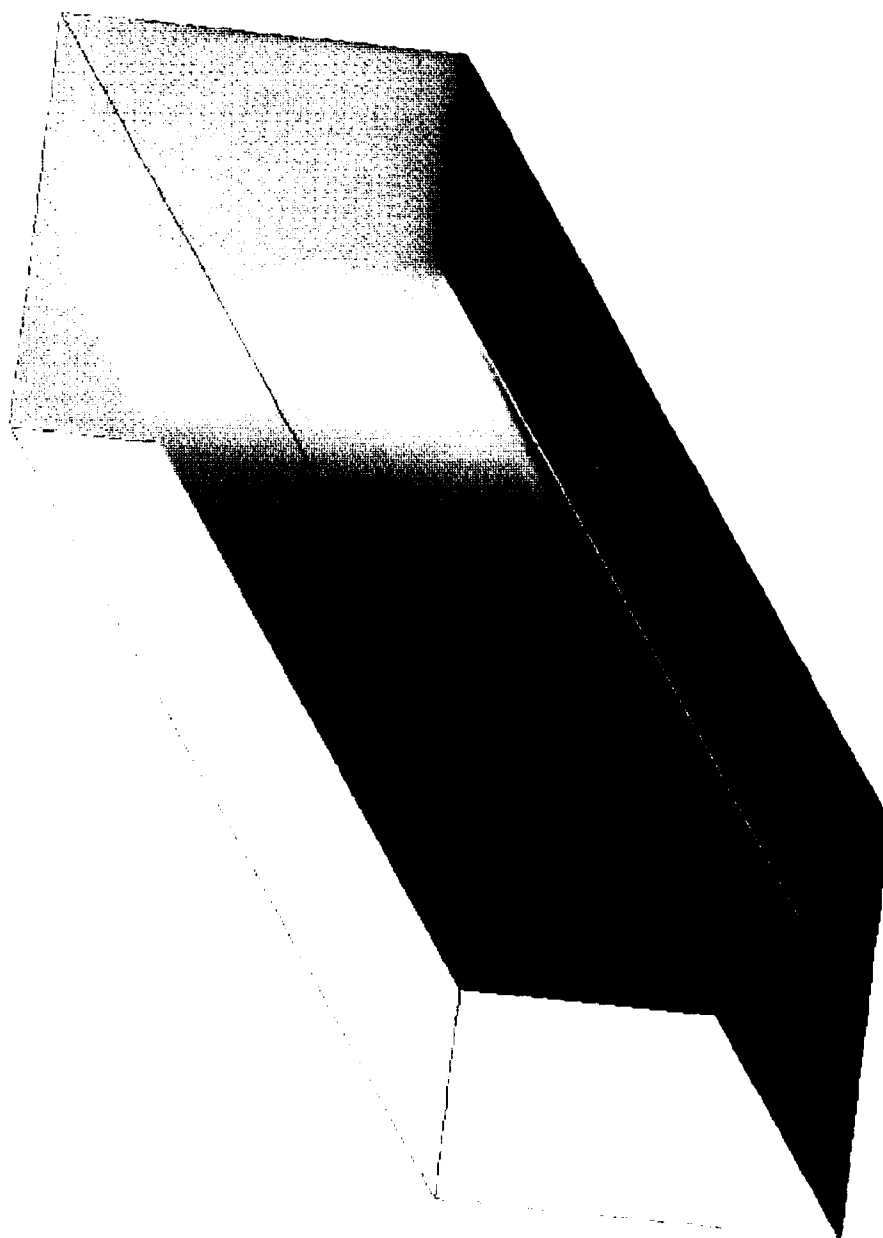


Figure 6-3. Density Distribution (kg/cu.m) in the Test Cell

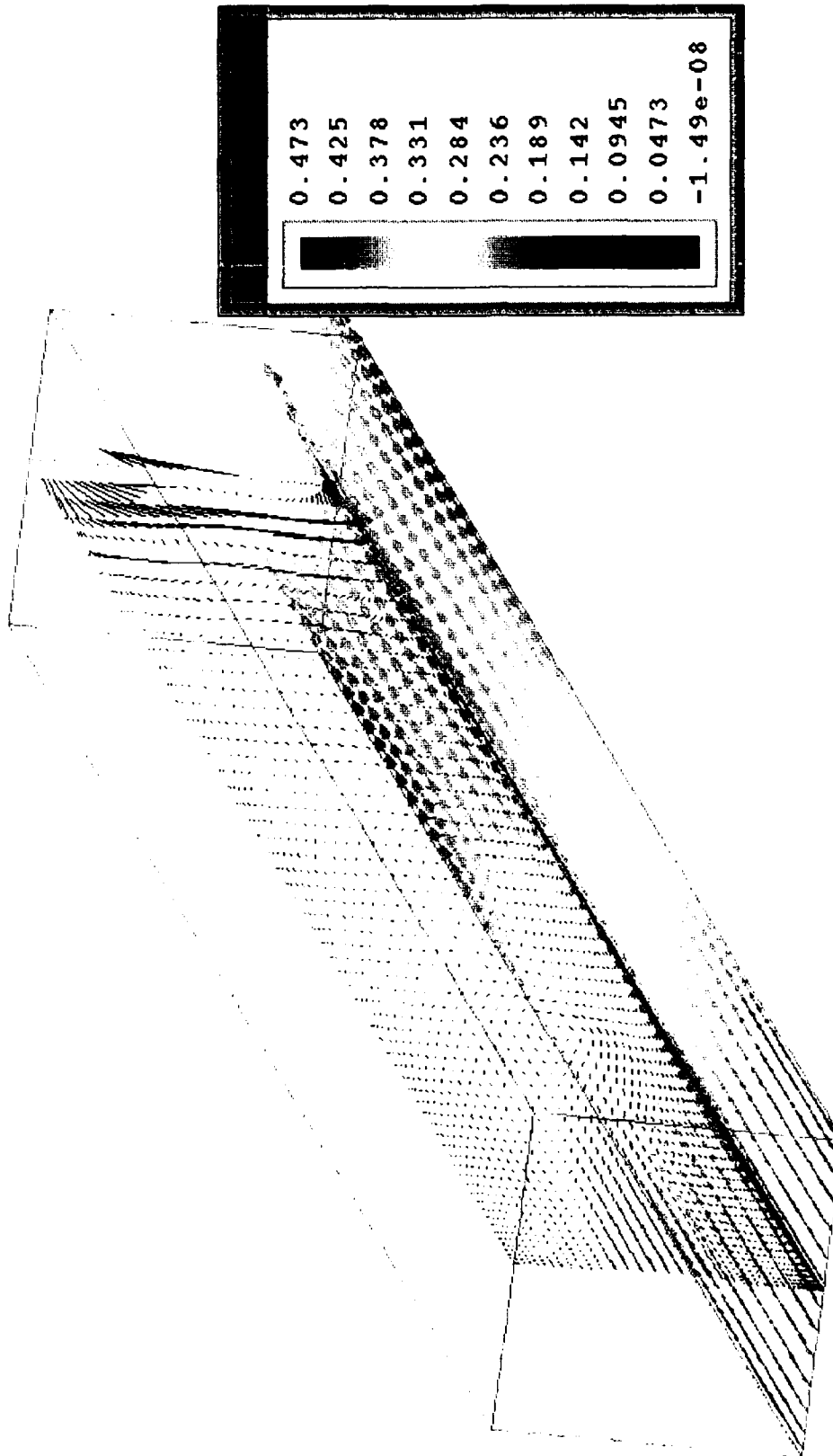


Figure 6-4. Velocity Field (m/sec) inside the Test Cell

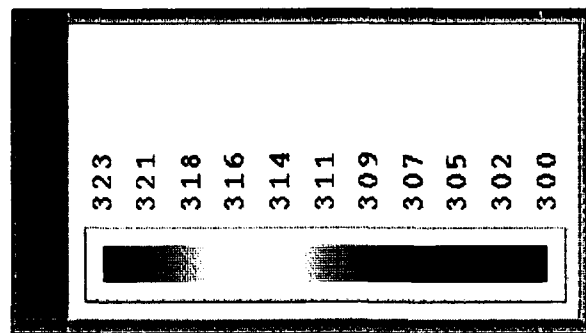
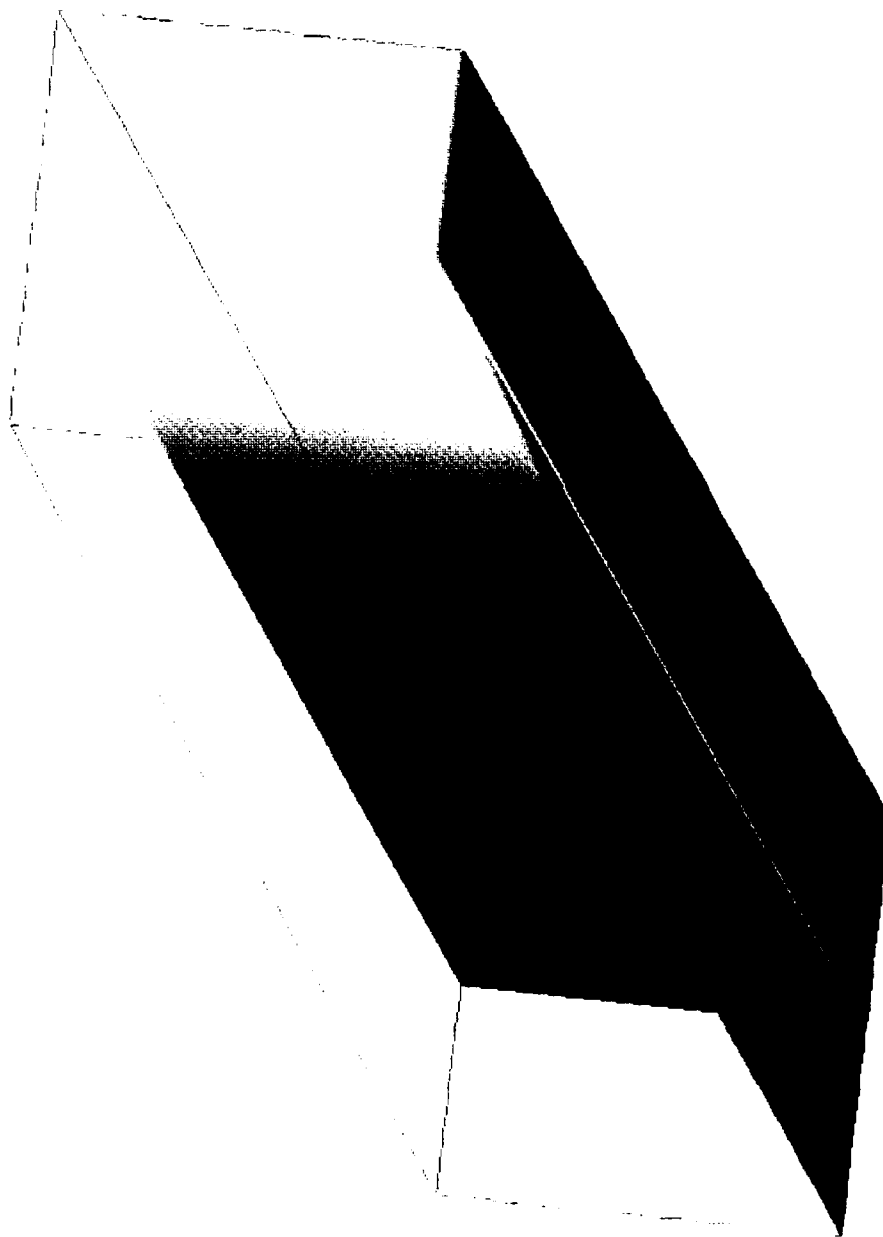


Figure 6-5. Temperature Distribution (degrees Kelvin) in the Test Cell

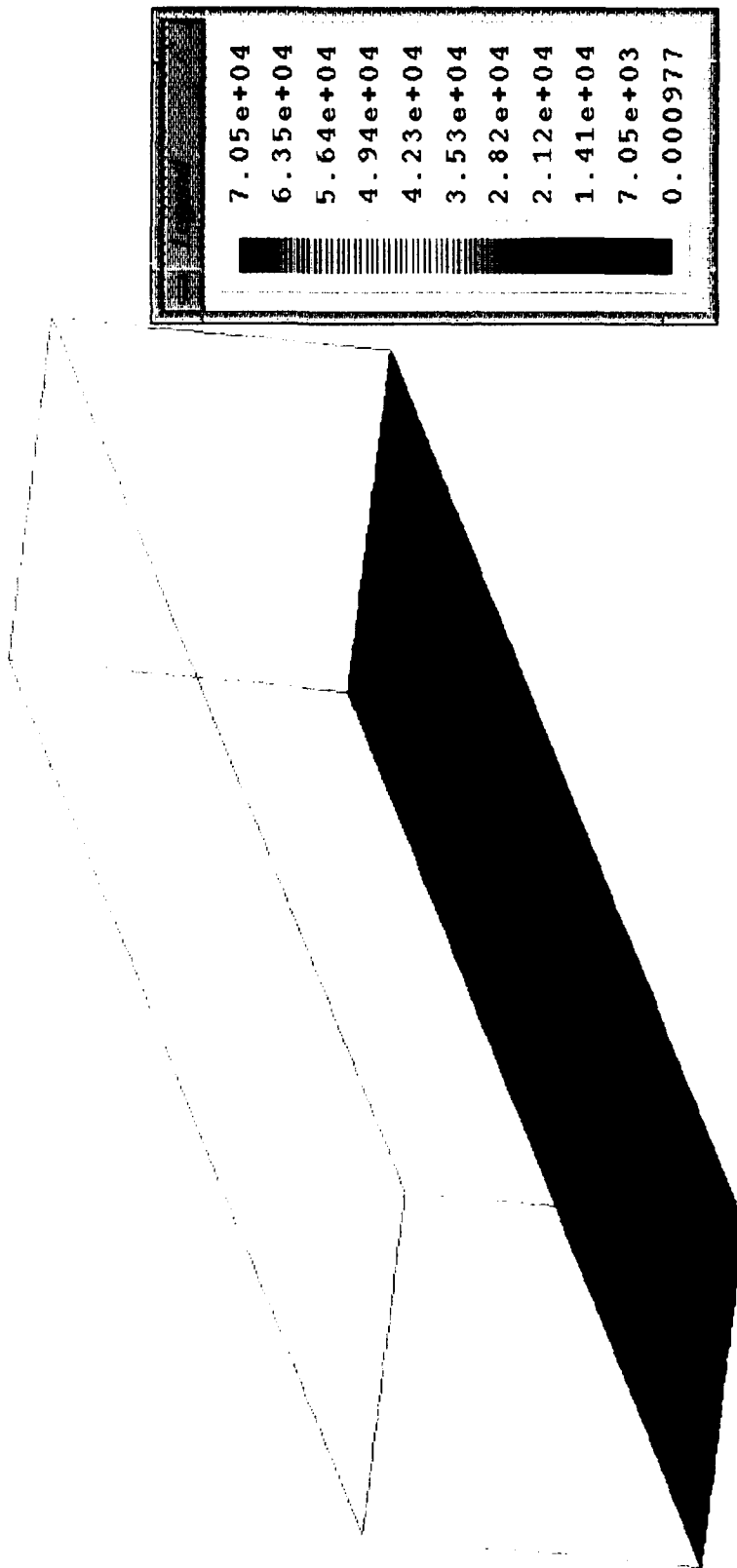


Figure 6-6. Heat Flux Distribution (J/sq.m-sec) on the Heated Surface

It is observed that supercritical phenomena manifest themselves in a complex manner in the flow field. It is difficult to understand the interactions between various physical mechanisms through experiments alone. The modeling of these flows yields considerable insight into the governing physical processes. Experiments are needed to judge the validity of the model and to guide model development. The current Phase I effort has demonstrated proof-of-concept that joint computational/experimental studies are crucial in order to develop and improve predictive capabilities for supercritical flows.

7. CONCLUSIONS AND RECOMMENDATIONS

This section summarizes the work performed, outlines the main findings of this study and presents recommendations for future work.

7.1 Summary of Work Performed

All of the objectives of the Phase I study have been met. The main accomplishments of the project are summarized below.

- a. **Development of Supercritical Transport Model:** A comprehensive model was formulated to calculate the transport properties of SF_6 as a function of local pressure, temperature and composition. This model was able to reproduce correctly the variation of these properties in the vicinity of the critical point.
- b. **Incorporation of Model into 2-D CFD Code:** The supercritical transport model was incorporated into a general purpose 2-D CFD code which was then used to perform heat transfer calculations in a channel. Wall heat fluxes were computed along the channel wall and compared with predictions from the ideal gas model. It was demonstrated in this study that the ideal gas model is highly inappropriate for modeling supercritical flows due to its inability to resolve the steep variations in properties around the critical point. The model was also used to study the relationship between dimensionless quantities such as the Nusselt number and the Reynolds number.
- c. **Assessment of Natural Convection Effects:** The steep variation in density around the critical point gives rise to strong buoyancy effects in low speed supercritical flows under laboratory conditions. One of the objectives of this study was to run the experiments at a low enough Reynolds number (to avoid turbulent flow situations) and yet prevent gravity driven flow instabilities from occurring within the test cell. The supercritical model was used to obtain the test cell orientation that best met these objectives. A vertical orientation of the test cell with the

flow going from the bottom to the top was found to minimize buoyancy driven instabilities.

- d. **Experiments with SF₆:** Experiments were carried out (as part of a subcontract) by Professor L. D. Chen at the University of Iowa. The flow inside the test cell was experimentally visualized in the subcritical, critical, and supercritical regimes. The results were presented in the form of shadowgraphs. The experimental data were used for preliminary validation of the model.
- e. **Incorporation of Model into 3-D CFD Code:** The supercritical fluid model was incorporated into a 3-D CFD code to simulate the flow in the test cell. Since the geometry of the test cell produces a 3-dimensional flow, a 3-D model was necessary for the simulations. The results of the simulations were compared with the data obtained from experiments.

The Phase I effort has resulted in the development of a novel and unique capability to simulate critical and supercritical flows using a general purpose CFD code. Therefore, the effect of complex boundary and operating conditions can be simulated without the use of adhoc empirical correlations.

7.2 Main Findings from the Phase I Study

Since the properties of supercritical fluids are strong functions of the local pressure, temperature and composition, it is necessary to incorporate supercritical models into CFD codes capable of resolving the interactions between these quantities. Phenomena such as heat transfer and chemical reactions are an outcome of these interactions. The results of this study show that heat transfer characteristics are altered by an order of magnitude due to supercritical effects. This behavior is certain to affect the temperature distribution in the test cell and hence the chemistry (through the non-linear dependence on temperature). It was also found that phenomena such as gravity should be given careful consideration in conjunction with supercritical fluids. The steep density gradients occurring in supercritical flows

may give rise to intrinsic flow instabilities under the influence of pressure gradients (hydrostatic and hydrodynamic).

The Phase I work has shown the proof-of-concept of coupling detailed supercritical fluid models with conventional CFD codes to predict flow and heat transfer characteristics. This approach provides the capability of analyzing the effects of complex boundary conditions on local flow behavior. It also provides a base for including more physical models for phenomena such as chemical reactions in order to study precombustion chemistry in jet fuels.

7.3 Recommendations for Phase II

In order to develop a general purpose capability to simulate the precombustion chemistry and transport phenomena in supercritical jet fuels, the following refinements are being considered for Phase II of this project:

- a. **Development of Multi-Component Capability:** The Phase I effort focused on the analysis of the supercritical behavior of SF_6 which was used as a surrogate fuel during this study. Jet fuels on the other hand are a complex mixture of various hydrocarbons. This requires the capability to model additional features such as multi-component diffusion, thermodiffusion (the Soret Effect), the Dufour Effect, etc. in the supercritical regime.
- b. **Development of Chemistry and Deposition Models:** The precombustion chemistry in jet fuels involves a range of complex processes such as (i) auto-oxidation of the fuel at low temperatures with the dissolved oxygen, (ii) thermal pyrolysis of the hydrocarbon molecules at higher temperatures, (iii) formation of insolubles such as gums, particles, *etc.*, (iv) transport and deposition of the insolubles on the walls of the fuel lines. It is necessary to develop models for the homogeneous gas phase reactions that give rise to the insolubles and the heterogeneous reactions that actually result in surface deposition. The study of particle formation should also include the analysis of homogeneous and heterogeneous nucleation.

- c. **Development of Turbulence Models for Supercritical Flows:** All of the modeling work in Phase I was done using laminar flow models. From practical considerations, it is necessary to be able to model turbulent supercritical flows. Existing models such as the k- ϵ turbulence model may require additional calibration in the supercritical regime. Special considerations must be given to the validity for the standard wall functions. Large eddy simulations may also be needed for understanding the nature of turbulence in these flows.
- d. **Analysis of Additives:** Anti-oxidants are added to the fuel to inhibit thermal oxidation that directly contributes to the formation of insolubles. Metal deactivators (MDAs) have also been used to reduce the catalytic activity of dissolved metals. However, at higher temperatures, the stability of these additives become a concern. The chemistry of the additives has to be understood in order to predict thermal stability. Accurate models have to be developed to simulate the effect of the additives over a range of conditions.
- e. **Validation with Benchmark Data:** The models developed during this study have to be validated against benchmark data. Since reliable data for many fluids in the supercritical regime are almost non-existent, it is necessary to design an experimental setup to perform appropriate experiments. The conditions prevailing inside jet fuel systems should be reproduced in the laboratory. Experiments need to be carried out to measure quantities that can be used to validate the computational models. Work is underway to identify candidate experimental sites for the Phase II work. Some of these are (i) University of Iowa, (ii) United Technologies Research Center in Hartford, CT, (iii) Pratt & Whitney, FL, and (iv) General Electric Aircraft Engines in Cincinnati, OH.

The details of these tasks will be presented in the Phase II proposal.

7.4 Phase III Objectives

For CFDRC, the potential applications of this work in Phase III include:

- a. Commercialization of the developed software for analyzing supercritical flows ;
- b. Commercialization of customized software for analysis of jet fuel systems with capabilities to model complex geometries such as heat exchangers, injector tubes, coils, *etc.*;
- c. Analysis and development of design correlations, novel concepts, and devices involving applications of supercritical flows; and
- d. Providing technical support and services to users.

Effort is currently underway to identify would-be commercial users of this product. Discussions are currently in progress with **Pratt & Whitney, Delavan, and GE Aircraft Engines** for collaborative work during Phase II and for potential Phase III (non-SBIR) commitments.

8. REFERENCES

1. Horvath, A.L., Physical Properties of Inorganic Compounds, Crane, New York, 1975
2. Reid, R.C., Prausnitz, J.M., and Poling, B.E., The Properties of Gases & Liquids, 4th edition, McGraw-Hill, New York, 1987.
3. Wark, K., Thermodynamics, 4th ed., McGraw-Hill, New York, 1983.
4. Bird, R.B., Stewart, W.E., and Lightfoot, E.N., Transport Phenomena, John Wiley & Sons, 1960.
5. Hall, W.B., "Heat Transfer Near the Critical Point," *Advances in Heat Transfer*, vol. 7, 1991.
6. Kreith, F., Principles of Heat Transfer, 3rd ed. Harper & Row, 1973.